SPATIAL ANALYSIS OF EVENT RELATED BRAIN POTENTIALS (ERP) BY WAVELET TRANSFORM

by

Ali Bayram

B.S., Electronic and Comm. Engineering, Yıldız Technical University, 2001

Submitted to the Institute of Biomedical Engineering
in partial fulfillment of the requirements
for the degree of
Master of Science
in
Biomedical Engineering

Boğaziçi University
2005

ACKNOWLEDGMENTS

I am deeply grateful to my thesis supervisor Assoc. Prof. Dr. Ahmet Ademoğlu and my thesis co-supervisor Prof. Dr. Tamer Demiralp for their kind academic support, supervision and motivation during this research with endless tolerance and patience.

I would like to thank my thesis committee members Assoc. Prof. Dr. Albert Güveniş, Assist. Prof. Dr. Ata Akın and Assist. Prof. Dr. Burak Güçlü for making valuable suggestions.

I would also like to thank Dr. Erol Yıldırım for providing me with the valuable EEG data.

Finally, I am deeply grateful to my family (Emine, H. Tahsin Bayram) for their continuous support not only for this thesis but for my whole life.

ABSTRACT

SPATIAL ANALYSIS OF EVENT RELATED BRAIN POTENTIALS (ERP) BY WAVELET TRANSFORM

Localization of the cognitive activity in the brain is one of the major problems in neuroscience. Current techniques for neuro-imaging are based on fMRI, PET, and ERP recordings. The highest temporal resolution, which is crucial for temporal localization of activities, is achieved by ERP, but spatial resolution of scalp topography is low. To overcome the limitation of scalp topography, several current-density estimation techniques were developed whose goal is to find the locations of the three-dimensional (3D) intracerebral activities by solving an inverse problem. However, scalp topologies constituted by multiple sources which makes the inverse problem more complicated. The overall objective of this thesis is to perform spatial analysis of scalp topography by 2-D wavelet transform and isolate spatial frequency components. This analysis could give us less complex scalp maps for source detection. In this thesis, in order to see the topographic variations in neurocognitive processes, the ERP recordings were spatially enhanced by interpolation as a first step. At the second step, main topologies of ERP recordings were investigated by hierarchical clustering algorithm. Thirdly, different spatial frequencies of these main topologies were separated by 2-D wavelet transform. Finally, main topological maps and topographic maps of different spatial frequencies derived from them were used to find corresponding cortical activities (cortical activity maxima) by LORETA (Low Resolution Electromagnetic Tomography). Assessment of our spatial analyzing results was made according to the current density estimation results.

Keywords: ERP, scalp topography, spatial analysis, 2-D wavelet, LORETA.

ÖZET

OLAY İLİŞKİLİ BEYİN POTANSİYELLERİNİN (OİP) UZAYSAL DALGACIK DÖNÜŞÜMÜ İLE ANALİZİ

Beyin içerisindeki kognitif aktivasyonların konumlandırılması, sinir biliminin önemli problemlerinden biridir. Varolan nörogörüntüleme tekniklerinin veri kaynaklarını ise fMRI, PET ve OİP kayıtları oluşturmaktadır. Aktivasyonların zamansal konumlandırılmasında hayati önem taşıyan zamansal hassasiyet, OİP kayıtları ile sağlanmakta fakat kafatası topografisinin çözünürlüğü düşük olmaktadır. Kafatası topolojisinin bu problemini aşmak için, birçok akım-yoğunluğu yaklaşımı geliştirilmiştir ki bunların amacı ters problem çözümü ile intraserebral aktivasyonların 3-B konumlarının bulunmasıdır. Ancak, kafatası topolojileri, ters problemi daha da karmaşık hale getiren çoklu kaynaklar tarafından oluşturulmaktadır. Bu tezin genel amacı, 2-B dalgacık dönüşümü yoluyla kafatası topolojilerinin yüzeysel analizini gerçekleştirmek ve yüzeysel frekans bileşenlerini ayrıştırmaktır. Bu analiz kaynak tesbiti için bize daha az karmaşık kafatası topolojileri sağlayabilir. İlk adım olarak bu tezde, olay ilişkili potansiyeller (OİP), nörokognitif süreçlerdeki topolojik dağılımları belirlemek için, interpolasyon ile yüzeysel olarak geliştirildi. İkinci adımda, hiyerarşik kümeleme algoritması ile OİP kayıtlarının temel topolojileri araştırıldı. Üçüncü olarak, bulunan temel topolojilerin farklı yüzeysel frekansları 2-B dalgacık dönüşümü ile ayrıştırıldı. Sonuçta, LORETA kullanılarak, temel topolojik haritalarına ve bunlardan elde edilen farklı yüzeysel frekans bileşenlerine karşılık gelen beyindeki aktivasyonlar bulundu. Uzaysal analiz sonuçlarının değerlendirilmesi, akım yoğunluk yaklaşımı sonuçlarına göre yapıldı.

Anahtar Sözcükler: OİP, kafatası topolojisi, yüzysel analiz, 2-B dalgacık, LORETA.

TABLE OF CONTENTS

LIST OF FIGURES

LIST OF TABLES

LIST OF SYMBOLS

$L_2(R)$	Square integrable signals
$\psi(t)$	Wavelet function
$\varphi(t)$	Scaling function

LIST OF ABBREVIATIONS

EEG	Electroencephalography
fMRI	functional Magnetic Resonance Imaging
PET	Positron Emission Tomography
ERP	Event Related Potentials
EOG	Electrooculogram
WT	Wavelet Transform
CWT	Continuous Wavelet Transform
DWT	Discrete Wavelet Transform
MW	Mother Wavelet
FIR	Finite Impulse Response
LORETA	Low Resolution Electromagnetic Tomography

1. INTRODUCTION

1.1 Motivation

Localization of the cognitive activity in the brain is one of the major problems in neuroscience. Electroencephalography is a convenient technique for studying and understanding cognitive activities of the brain.

The most important property of the EEG, which makes it superior to other neuro-imaging modalities such as fMRI or PET, is its very high temporal resolution. Cognitive information processing seems to consist of multiple individual stages each lasting from 50 to 300 ms. EEG reflects functional activities in the range of milliseconds. However, fMRI or PET is used to survey the entire brain for localized changes in glucose metabolism or blood flow that follow neural activity in cognitive tasks. Consequently, fMRI or PET is limited by the indirect and temporally-delayed relation between metabolism and synaptic currents which may result about one minute delay [1]. Another advantage of EEG is its non-invasive nature.

The main disadvantage of the EEG signals that are taken from the human scalp via electrode arrays is their complex potential distribution (Figure 3.6). It is known that, during stimulus processing in the brain, summated time courses of neural events constitute event-related potentials (ERPs). That is, ERPs do not reflect a single type of cognitive operation. Many different generator configurations in the brain could interfere the ERP topography at the scalp. Indeed, consecutive overlapping, and partly overlapping processes have been demonstrated to accompany ERP generation [2]. Moreover, overlapping may occur in time, frequency and space or any combinations of these domains.

The development of powerful time-frequency analysis techniques such as Wavelet Transform (WT)[3], [4], [5] in recent years made the characterization of the time-

varying frequency characteristics of ERPs possible [6], [7], [8].

In the case of spatial decomposition, there are constraints based on low spatial resolution of ERP recordings, because recordings are taken from scalp surface but sources that generate electric currents are in the brain. Furthermore, two-dimensional scalp topography restricted to a small number of electrodes, might provide low or somewhat distorted information on the source location. To overcome the limitation of scalp topography, several current-density estimation techniques are developed whose goal is to find the location of the three-dimensional (3D) intracerebral activities by solving an inverse problem. Among several available methods, LORETA (Low Resolution Electromagnetic Tomography) is one of the most widely used methods for the solution of inverse problems. LORETA, using a realistic head model of the boundary element method derived from the individual anatomy, estimates the current density maps from the scalp topography [9].

1.2 Objectives

In this thesis, the ERP signals are analyzed by 2-D wavelet transform in order to study the spatio-temporal components which may correspond to different cognitive processes. This analysis is made to separate the spatial frequency components of a particular or dominant temporal topography in the ERP signal which is assumed to be correlated to a single or multiple cognitive processes during ERP generation.

The ERPs (30 channels) which are recorded during the widely used neurophysiological test: Stenberg Working Memory Paradigm (with verbal recognition variants), is studied. The first aim is to find main topologies of ERP recordings by hierarchical clustering algorithm. After developing 2-D wavelet based spatial frequency analyzing toolbox, main topologies are divided in to spatial frequency components. Conclusive purpose is to detect corresponding cortical activities of different spatial frequency components and main topologies via LORETA. Results are assessed if they have a supportive prospect due to our initial assumption of connection between spatial frequency

components of scalp recordings and cortical activities in the brain.

1.3 Outline of the Thesis

The background of the relevant concepts is described in the second chapter. This chapter briefly includes, EEG and ERP signals, cognitive paradigm that is used and the theory behind the wavelet transform.

Chapter 3 covers detailed description of ERP recordings and experimental design. Spatial enhancement of ERP recordings by a spline based interpolation technique in order to see the topographic variations (two-dimensional) in neurocognitive processes is also described.

Chapter 4 contains the investigation of main topologies of ERP recordings by hierarchical clustering algorithm and different spatial frequencies of these main topologies are separated by 2-D wavelet transform. The cluster trees and topographic scalp maps are calculated and demonstrated by the developed toolboxes (Appendix A, B).

In Chapter 5, there is a LORETA application to find corresponding cortical activities of main topological maps and their spatial wavelet analysis results. Locations of activations are also demonstrated by tables.

Assessment of findings is made in Chapter 6. Effect of spatial frequency separation on source localizations is also discussed.

Chapter 7 is the conclusion part of the thesis which explains the limitations, difficulties, and advantages of spatio-temporal analysis of event related brain potentials.

Appendixes contains a brief user manual of the developed toolboxes.

2. BRAIN POTENTIALS AND WAVELET TRANSFORM

2.1 Electroencephalogram (EEG)

EEG is an important tool in studying the brain activity and investigating the mental processes. Hans Berger reported the first measurement of brain electrical activity in humans in 1924. He demonstrated that the shape and frequency of EEG waveforms depended on the state of the brain, and then one of the most important diagnostic tools of neurophysiology, most notably in epilepsy, emerged. EEG recordings are achieved by placing highly conductive electrodes (Z_e less than 5 $K\Omega$) in specific locations of the head. Measures of the electric potentials can be recorded between pairs of active electrodes (bipolar recordings) or with respect to a supposed passive electrode called reference (monopolar recordings). These measures are mainly performed on the surface of the head (scalp EEG).

The intensities of the brain waves on the surface of the brain (recorded relative to an indifferent electrode such as the earlobe) may be as large as 10 mV, whereas those recorded from the scalp have smaller amplitude of approximately 100 μV. The frequencies of these brain waves range from 0.5 to 100 Hz, and their character is highly dependent on the degree of activity of cerebral cortex [10].

2.2 Definition of ERP

Event-related potentials (ERPs) are the electrical response of the brain to an external stimulus (Figure 2.1). The amplitude of ERP peaks are usually under 5 μV and rarely exceeding 10 μV. This makes the ERP peaks far smaller than the spontaneous activity which has typical amplitude of 20 - 50 μV.

ERPs have proven to be an invaluable asset to cognitive research. Analysis of

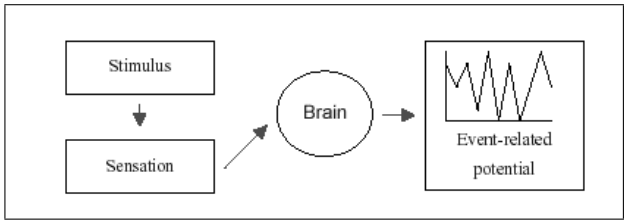

Figure 2.1 Origin of the ERP signals.

different ERPs gives clues about the way in which the brain processes information. ERPs have revealed that seemingly alike processes are handled at different locations in the brain. Other research tools fail to produce information about the order of the processing sequences and their timings. It is believed that the brain has separate input and output utilities. Distinct central processing occurs between these input and output sequences. Many scientists hope that ERPs will shed light onto the phenomenon of consciousness. ERPs have great potential for clinical use. ERPs can not only be used for the early detection of neurological diseases, but also for the classification of patients into disease subtypes. Among their countless possible uses is the monitoring of the progress or deterioration of an elderly or demented patient.

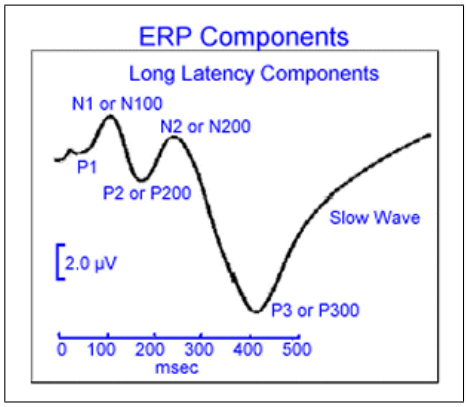

Figure 2.2 ERP components.

The ERP components are written with a specific notation (Figure 2.2). They begin with a capital letter designating the polarity of the peak. This is followed by a number that designates peak's approximate delay from the stimulus.

2.3 Wavelet Transform

2.3.1 Continuous Wavelet Transform (CWT)

A decomposition of square integrable signals $L_2(R)$ are developed under the name of wavelets [3].

A continuous wavelet transform (CWT) maps a time function into a two-dimensional function of a and b, where a is the scale (1/a denotes frequency) and b is the time translation [11]. For a signal x(t), the CWT can be written as follows:

$$W(a,b) = a^{-1/2} \int_{-\infty}^{\infty} x(t) \cdot \psi^*(\frac{t-b}{a}) \cdot dt \tag{2.1}$$

where, $\psi(t)$ is a mother wavelet (MW), $\psi^*_{a,b}(t)$ denotes the complex conjugate of $\psi_{a,b}(t)$, and $\psi_{a,b}(t)$ stands for a wavelet basis function (Eq. 2.2).

$$\psi_{a,b}(t) = a^{-1/2} \cdot \psi(\frac{t-b}{a}) \quad a,b \in R \quad a \neq 0 \tag{2.2}$$

The MW, $\psi(t)$is an oscillatory function whose Fourier transform $\widehat{\psi}(\omega)$ must satisfy the following admissibility condition:

$$C_\psi = \int_{-\infty}^{\infty} \frac{|\widehat{\psi}(\omega)|^2}{|\omega|} d\omega < \infty \tag{2.3}$$

$$|\widehat{\psi}(\omega)|^2|_{\omega=0} = 0 \tag{2.4}$$

If this condition is satisfied, $\psi(t)$ has zero mean, and the original signal can be recovered from its transform $W(a,b)$ by the inverse transform (Eq. 2.5)

$$x(t) = \frac{1}{C_\psi} \int_{-\infty}^{\infty} \int_{-\infty}^{\infty} W(a,b) a^{-1/2} \psi(\frac{t-b}{a}) \frac{dadb}{a^2} \tag{2.5}$$

2.3.2 Discrete Wavelet Transform

Discrete wavelets are not continuously scalable and translatable but can only be scaled and translated in discrete steps. This is achieved by modifying the wavelet representation as

$$\psi_{j,k}(t) = 2^{-j/2}\psi(2^{-j}t - k) \tag{2.6}$$

In Eq. 2.6, the variables j and k are integers that scale and dilate the mother function $\psi(t)$ to generate wavelets. The scale index j indicates the wavelet's width, and the location index k gives its position. Because of the 2^j, the sampling of the frequency axis corresponds to dyadic sampling.

If we look at Eq. 2.4, we see that the wavelet has a band-pass like spectrum. From Fourier theory we know that compression in time is equivalent to stretching the spectrum and shifting it upwards (Figure 2.3).

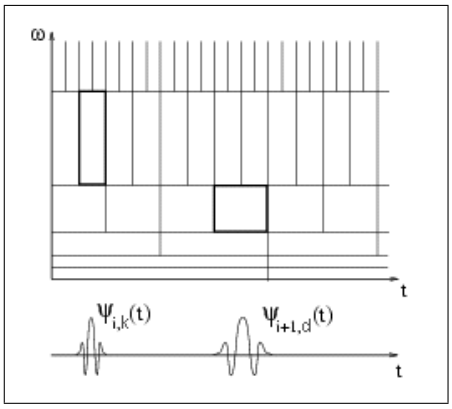

Figure 2.3 The time frequency boxes of a wavelet basis define a tiling of the time-frequency plane.

$$F\{f(at)\} = \frac{1}{|a|}F(\frac{\omega}{a}) \tag{2.7}$$

Using this insight we can cover the finite spectrum of our signal with the spectra of dilated wavelets in the same way as that we covered our signal in the time domain with translated wavelets. To get a good coverage of the signal spectrum the stretched wavelet spectra should touch each other, as if they were standing hand in hand. This

can be arranged by correctly designing the wavelets.

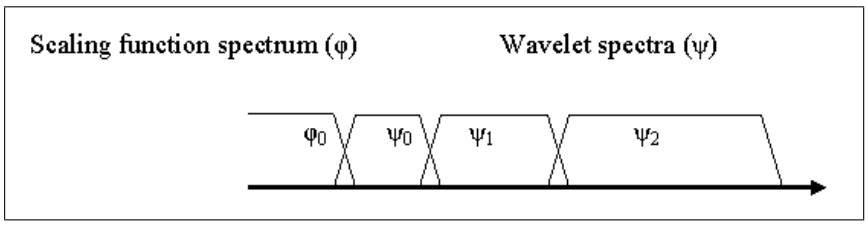

Figure 2.4 Touching wavelet spectra resulting from scaling of the mother wavelet.

With every wavelet stretch, we cover only half of the remaining spectrum, which means that we need low-pass spectrum so-called scaling function in order to cover all spectra (Figure 2.4).

If we look at the scaling function as being just a signal with a low-pass spectrum, then we can decompose it in wavelet components and express it like:

$$\varphi(t) = \sum_{j,k} \gamma(j,k)\psi_{j,k}(t) \tag{2.8}$$

This is constructed by summing wavelets weighted by coefficients.

In Eq. 2.8, we stated that the scaling function could be expressed in wavelets from minus infinity up to a certain scale j. If we add a wavelet spectrum to the scaling function spectrum we will get a new scaling function, with a spectrum twice as wide as the first. The effect of this addition is that we can express the first scaling function in terms of the second, because all the information we need to do this is contained in the second scaling function. We can express this formally in the so-called multiresolution formulation [12] or two-scale relation [13]:

$$\varphi(2^j t) = \sum_k h_{j+1}(k)\varphi(2^{j+1}t - k) \tag{2.9}$$

The two-scale relation states that the scaling function at a certain scale can be expressed in terms of translated scaling functions at the next smaller scale.

The first scaling function replaced a set of wavelets and therefore we can also

express the wavelets in this set in terms of translated scaling functions at the next scale. More specifically, we can write for the wavelet at level j:

$$\psi(2^j t) = \sum_k g_{j+1}(k)\varphi(2^{j+1}t - k) \tag{2.10}$$

Since our signal $f(t)$ could be expressed in terms of dilated and translated wavelets up to a scale $j-1$, this leads to the result that $f(t)$ can also be expressed in terms of dilated and translated scaling functions at a scale j:

$$f(t) = \sum_k \lambda_j(k)\varphi(2^j t - k) \tag{2.11}$$

In this equation, if we step up a scale to $j-1$, we have to add wavelets in order to keep the same level of detail. We can then express the signal $f(t)$ as

$$f(t) = \sum_k \lambda_{j-1}(k)\varphi(2^{j-1}t - k) + \sum_k \gamma_{j-1}(k)\psi(2^{j-1}t - k) \tag{2.12}$$

If the scaling function $\varphi_{j,k}(t)$ and the wavelets $\psi_{j,k}(t)$ are orthonormal or a tight frame, then the coefficients $\lambda_{j-1}(k)$ and $\gamma_{j-1}(k)$ are found by taking the inner products.

$$\lambda_{j-1}(k) = \langle f(t), \varphi_{j,k}(t)\rangle \quad \gamma_{j-1}(k) = \langle f(t), \psi_{j,k}(t)\rangle \tag{2.13}$$

If we now replace $\varphi_{j,k}(t)$ and $\psi_{j,k}(t)$ in the inner products by suitably scaled and translated versions of Eq. 2.9, Eq. 2.10 and manipulate a bit, keeping in mind that the inner product can also be written as an integration, we arrive at the important result:

$$\lambda_{j-1}(k) = \sum_m h(m-2k)\lambda_j(m) \tag{2.14}$$

$$\gamma_{j-1}(k) = \sum_m g(m-2k)\gamma_j(m) \tag{2.15}$$

These two equations state that the wavelet and scaling function coefficients on a certain scale can be found by calculating a weighted sum of the scaling function coefficients from the previous scale.

As we know from signal processing theory a discrete weighted sum like the ones in Eq. 2.14 and Eq. 2.15 is the same as a digital filter and since we know that the coefficients $\lambda_j(k)$ come from the low-pass part of the splitted signal spectrum, the weighting factors $h(k)$ in Eq. 2.14 must form a low-pass filter. Since we know that the coefficients $\gamma_j(k)$ come from the high-pass part of the splitted signal spectrum, the weighting factors $g(k)$ in Eq. 2.15 must form a high-pass filter. This means that, Eq. 2.14 and Eq. 2.15 together form one stage of an iterated digital filter bank (Figure 2.5) and from now on we will refer to the coefficients $h(k)$ as the scaling filter and the coefficients $g(k)$ as the wavelet filter.

By now we have made certain that implementing the wavelet transform as an iterated digital filter bank is possible and from now on we can speak of the discrete wavelet transform or DWT [14].

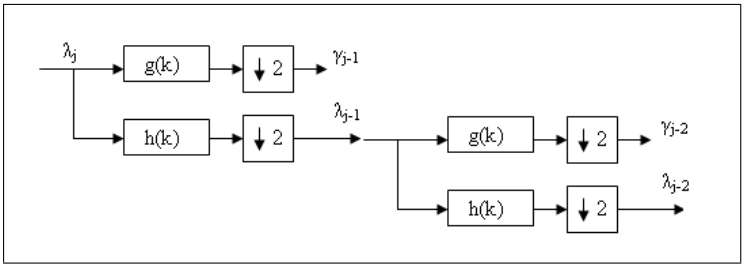

Figure 2.5 Implementations of Eq. 2.14 and Eq. 2.15 as two stages of an iterated filter bank.

2.3.3 Two-Dimensional Wavelets

The usual two-dimensional wavelets are defined as tensor products of one-dimensional wavelets: $\varphi(x, y) = \varphi(x)\varphi(y)$ is the scaling function. $\psi_1(x, y) = \varphi(x)\psi(y)$, $\psi_2(x, y) = \psi(x)\varphi(y)$ and $\psi_3(x, y) = \psi(x)\psi(y)$ are the three wavelets.

In a two-dimensional context, we have the translation by vector (b_1, b_2) and a change of scale of parameter (a_1, a_2). Translation and change of scale become:

$$\frac{1}{\sqrt{a_1 a_2}}\psi(\frac{x_1 - b_1}{a_1}, \frac{x_2 - b_2}{a_2}) \tag{2.16}$$

where, $(x = (x_1, x_2) \in R^2)$

This formulation is a two dimensional version of Eq. 2.2. Remaining equations can be converted to two dimensional versions by the same way. The following charts (Figure 2.6, Figure 2.7) describe the basic decomposition and reconstruction steps for images which is also described by Mallat [4]:

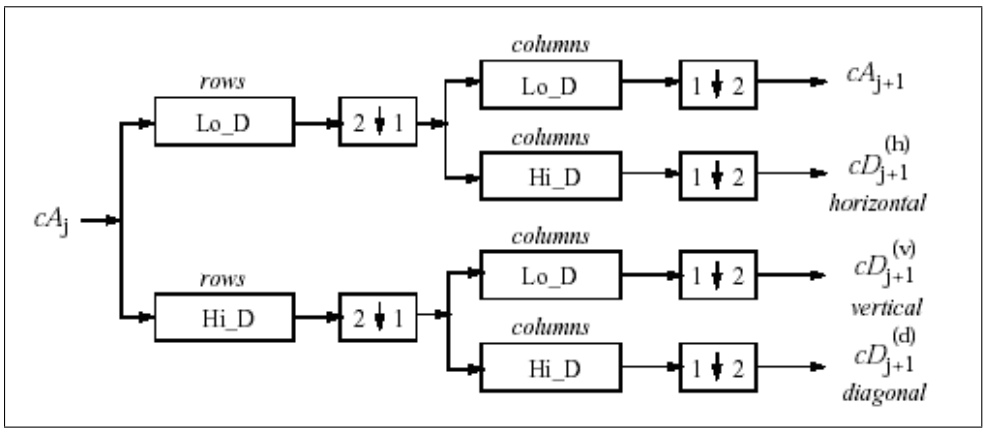

Figure 2.6 Two dimensional DWT, decomposition step.

where,

$\boxed{2 \downarrow 1}$ Downsample columns: keep the even indexed columns

$\boxed{1 \downarrow 2}$ Downsample rows: keep the even indexed rows

rows

X Convolve with X the rows of the entry

columns

X Convolve with X the columns of the entry

Initially cA_j = s for decomposition.

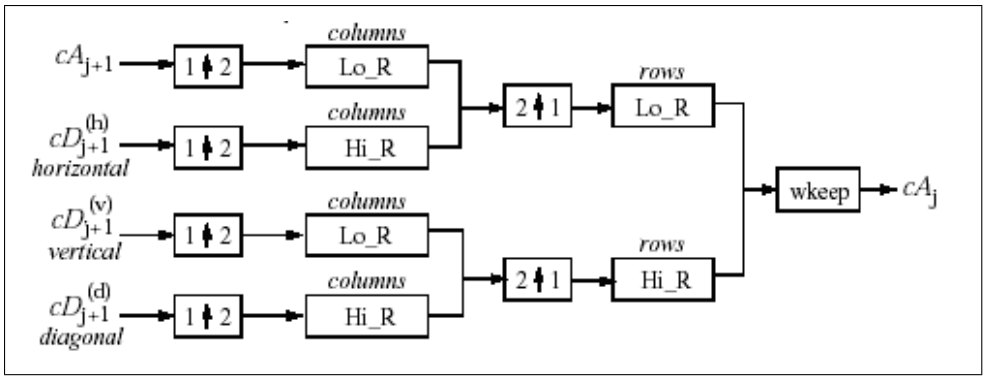

Figure 2.7 Two dimensional IDWT, reconstruction step.

Where,

$\boxed{2 \uparrow 1}$ Upsample columns: insert zeros at odd-indexed columns

$\boxed{1 \uparrow 2}$ Upsample rows: insert zeros at odd-indexed rows

wkeep Take the central part of the union matrix with the convenient length (power of 2)

rows

X Convolve with X the rows of the entry

columns

X Convolve with X the columns of the entry

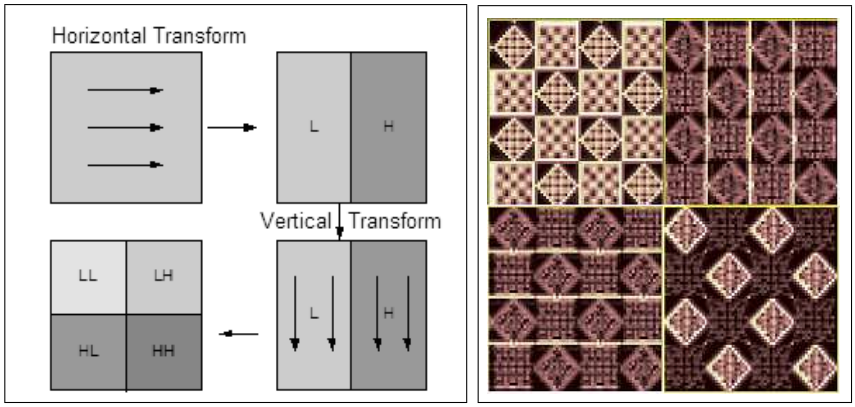

Figure 2.8 Illustration of two dimensional WT (left) and an example implementation (right)

Figure 2.8 illustrates (left) one level 2-D wavelet decomposition step, where "L" denotes low-pass filter and "H" denotes high-pass filter results. After decomposition, we have one approximation (LL) and three detail (HL: Horizontal, LH: Vertical, HH: Diagonal) coefficients.

Detail coefficients and approximation coefficients can be used to reconstruct images. If the decomposition is orthogonal, the image is decomposed by wavelet analysis into information that is independent from one scale to another. Reconstruction can be done by using approximation coefficients, single detail coefficient or all detail coefficients of the same scale.

3. ERP RECORDINGS AND TOPOGRAPHIC SCALP MAPS

3.1 Cognitive Paradigm

3.1.1 Sternberg Working Memory Paradigm

The Sternberg working memory is named after Saul Sternberg and is a paradigm to study short-term memory. The task consists of presenting participants with a number of letters, some of which (but not necessarily all) are marked to show that they have to be remembered for later recognition. After a brief retention period, a single probe letter is presented and the participants have to press a button if the probe was marked as a to-be-remembered item among the previously presented set of letters. Load can be varied by the number of items that are marked as to-be-remembered.

3.1.2 Stimulus Procedure of the Experiment

The Sternberg working memory test was performed during the experiment. White color letters (dark grey background) with the size of 3x3 cm were shown to subjects on a 15 inch computer screen as a stimulant set (Figure 3.1). Time interval between the appearances of two consecutive stimuli was 2 seconds and each stimulus lasted 1 second on the screen. The experiment started with the caution on the screen: "aklında tut!" which means "bear in mind!". After the letters had been presented as the memory set (three letters) the second caution "hatırla!" which means "recall!" was shown on the screen. After the caution, test stimuli were started. Time interval between two stimuli was again 2 seconds. Test stimuli include memory set letters (target) and distracter letters and the probability was arranged to be 50 % in all sessions. Subjects were exposed to 135 stimuli during each paradigm (45 memory set, 45 target stimuli, and 45 distracters). Subjects responded to 90 stimuli which include target and

distracter ones.

Subjects were instructed to press left mouse button as fast and accurate as possible, whenever the letters in the memory set was shown. If the letter shown on the screen was not in the memory set, pressing right mouse button in addition to that neglecting wrong answering was instructed to subjects before the test. The experiment whose memory set includes three letters was performed with 18 healthy volunteers.

Subjects' true, false, false positive and false negative responses were recorded. EEG recordings of memory set, target and distracter stimulant sets were separately analyzed. Target stimulant set recordings were used during the analysis in this thesis.

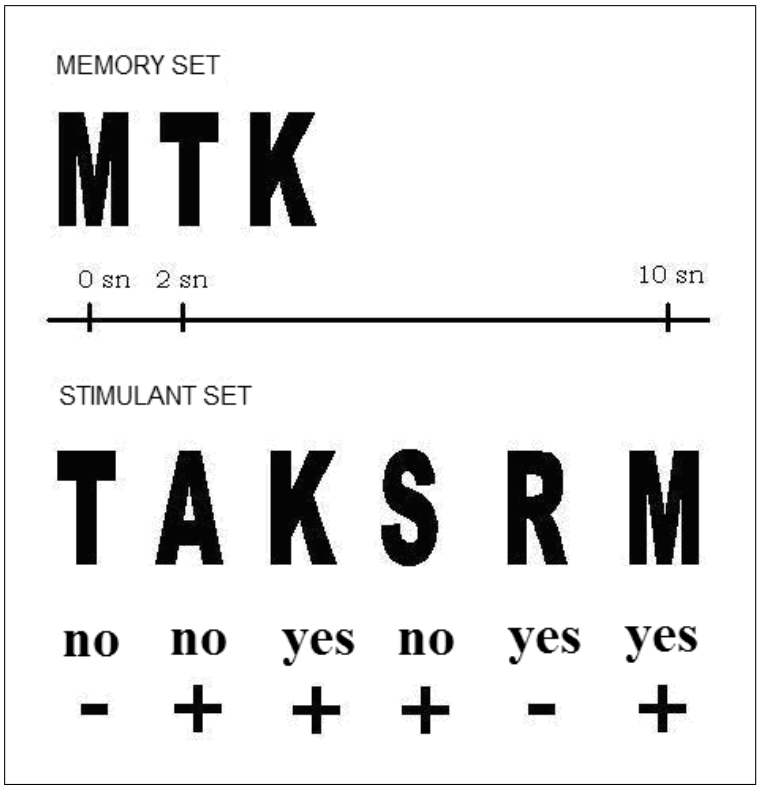

Figure 3.1 Memory set, test stimuli, example responses (yes : left mouse button press, no : right mouse button press) and results of responses (+ : true response, - : wrong response).

3.2 ERP Recordings

ERP recordings were taken from the subjects in an electrically shielded, sound-diminished, and dimly illuminated room at the Department of Physiology, Istanbul Medical Faculty, Istanbul University by Dr. Erol Yıldırım. Subjects were sitting on a comfortable chair during the sessions and distance between subject and the computer screen was arranged to 60 cm. Subjects responded to stimuli by using two buttons of a computer mouse.

Event related potentials were recorded from electrodes located according to extended international 10/20 system (Figure 3.2).

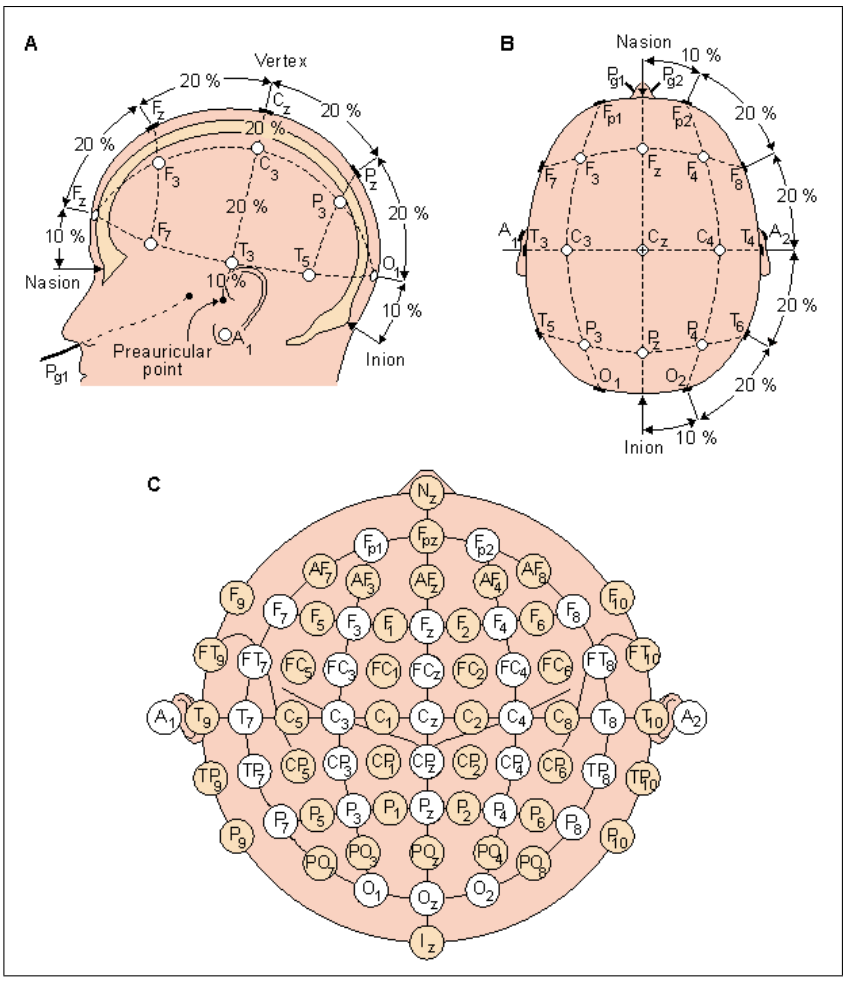

Figure 3.2 A, B: Electrode locations of International 10/20 system. C: Selected electrode locations(white color) from extended 10/20 system.

The data were collected by 30 electrodes: F_{p1}, F_{p2}, F_z, F_3, F_4, F_7, F_8, FC_z, FC_3, FC_4, CP_z, CP_3, CP_4, FT_7, FT_8, TP_7, TP_8, O_z, O_1, O_2, P_z, P_3, P_4, P_7, P_8 , C_z, C_3, C_4, T_7, T_8. Average value of grounded two more earlobe electrode (A_1, A_2) potentials was used as a reference of unipolar recordings (Figure 3.2).

Bridge electrodes were wetted by KCl solution and conductive liquid was used for cup electrodes. EOG recordings were made from eye-over and right eye in order to watch artifacts produced by eye movements.

Continuous ERPs were recorded digitally via a 32-channel EEG device (La Mont Medical Inc.). Impedances of the electrodes were kept below 20 kΩ. 0.1 Hz high-pass and 70 Hz low-pass filters were applied and recorded with 200 frame per second sampling rate to the computer.

After filtering the data, manual artifact elimination procedure, based on the reviewing of single ERP trials was applied. Finally, single ERP trials were averaged off-line in order to obtain the individual averaged ERPs. Individual ERPs are constituted by 500 msec pre-stimulus and 1 sec post-stimulus recordings (300 time frames). We can show signals obtained from each channel (Figure 3.3).

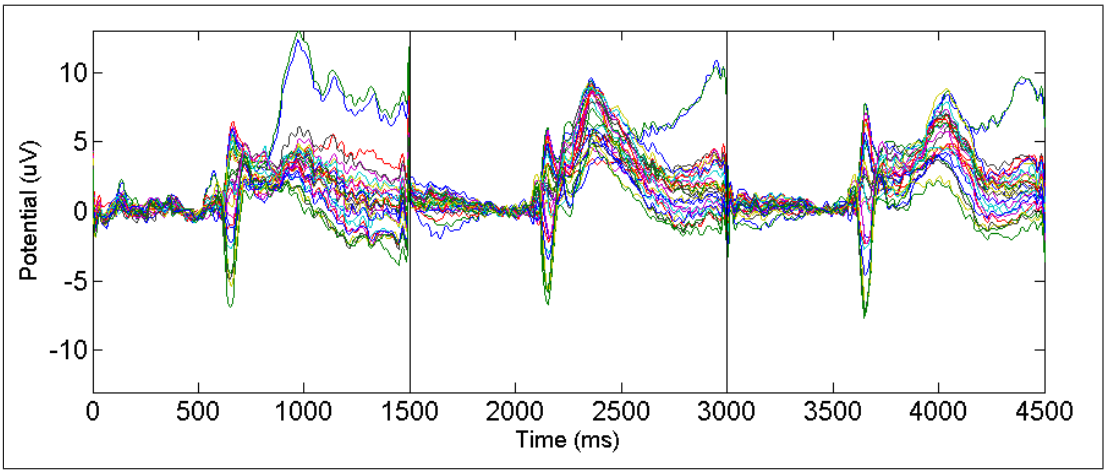

Figure 3.3 30 channel, three manually cascaded ERP recordings (1.5 sec = 300 frames) of different sessions.

3.3 The Topographic Mapping of Scalp Surface

In order to see the local topological variations, initially the recorded potentials need to be spatially enhanced. Typically, this is done with interpolation techniques. In this study, biharmonic spline interpolation technique is used as a tool for performing spatial enhancement of ERP recordings and constructing scalp maps.

Firstly, scalp surface is not a regular grid moreover distribution of the electrodes on the scalp is based on International 10/20 System, which also does not match a regular grid (see Figure 3.4). Secondly, image has to be enhanced with a possible lowest image distortion. At this point, spline based interpolation techniques can give successful results. Biharmonic spline interpolation technique satisfies both of them. It can be applied to irregularly placed data points and equivalent to cubic spline in two dimensions [15].

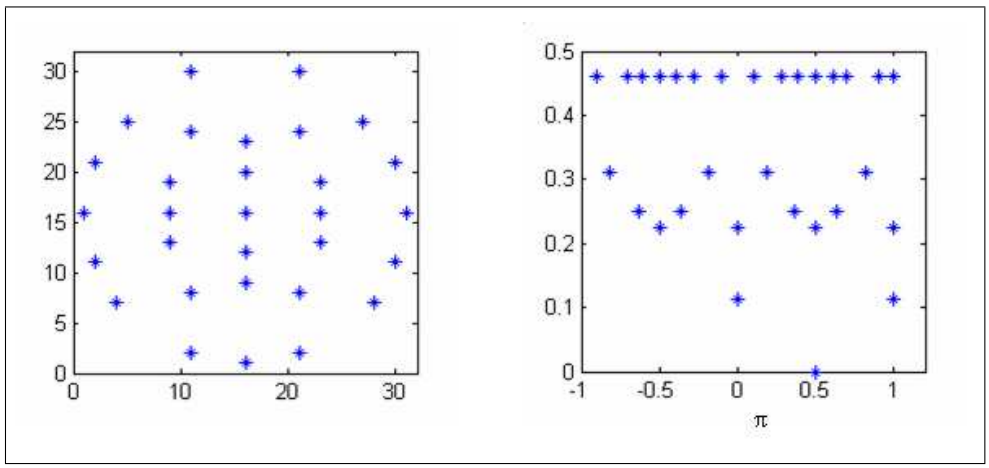

Figure 3.4 Cartesian (left), Polar (right) sensor locations on scalp.

As an input value of the interpolation, resolution of the scalp maps has to satisfy another criterion at wavelet analyzing step. To apply discrete wavelet techniques, spatially enhanced ERP frames (scalp maps) need to have dimensions with the power of 2. Selecting low scale for interpolation results in low resolution scalp maps, which can be a restriction for spatial analysis. On the other hand building high resolution scalp maps results in smooth scalp maps. However, in addition to long lasting calculation procedure high resolution produces much more synthetic data. In our case,

one dimension of the square scalp map contains 2^5 data points, which is enough for applying spatial analysis, produces visually enough resolution (see Figure 3.5) and does not consume too much processing time.

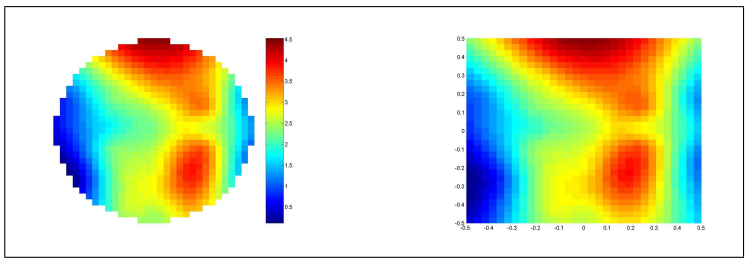

Figure 3.5 Interpolated (right) and Masked (left) brain maps (at 215 msec) constructed with interpolation. Seen from above, nose up.

After the interpolation, scalp maps are masked for the sake of visual assistance to the observer (Figure 3.5). This is done by replacing the data which is located outside of the scalp circle with zero. In Figure 3.5 (left) up is the front and down is the back of the head. This procedure is applied via toolbox for time frames which are obtained at each 5 *msec*. An example implementation can be seen in Figure 3.6.

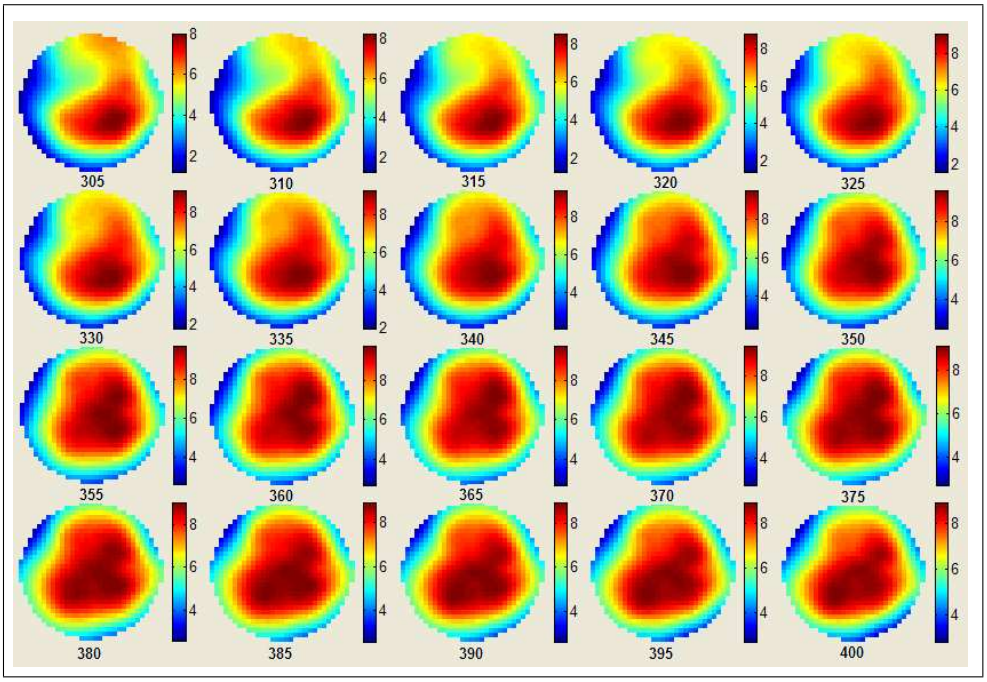

Figure 3.6 Example interpolated brain map sequence of 305-400 msec time interval with 5 msec steps.

4. MAIN TOPOLOGICAL SCALP MAP DETECTION AND SPATIAL WAVELET ANALYSIS

ERP recordings are the summation of signals from many sources and many different processes over the brain. This complex structure of the data produces complex and high variety scalp map topologies beside known patterns. In spite of applying spatial wavelet analysis to all sequence and assessing the results one by one, we tried to find out time windows within the recordings which include expected neuro-anatomical patterns. Thanks to cluster analysis, we could reduce variety by investigating temporal stationary topographies of scalp maps in order to apply spatial analysis.

4.1 Hierarchical Cluster Analysis

Hierarchical clustering is a way to investigate grouping in the ERP recordings (time frames), simultaneously over a variety of scales, by creating a cluster tree (see Figure 4.1). The cluster tree is not a single set of clusters, but rather a multilevel hierarchy, where clusters at one level are joined as clusters at the next higher level. This allows us to decide what level or scale of clustering is appropriate for us to select stationary topologies.

Hierarchical clustering is based on the assumption of independence of each pair (each time frame in our case) in a data set. That's why, pairs do not necessarily have to be temporally consecutive within a cluster after the clustering process. However, main property of cluster hierarchy of time frames must be their temporally consecutive nature, because different processes at different time courses may occur with the same topology produced by different sources. Selecting temporally consecutive time frames in the same hierarchical cluster could ensure separating different processes. In addition to that, if clustering technique could construct clusters with consecutive time frames without any interference, this validates the success of the technique to some extent. In

the light of this consideration we did not use any restriction during clustering.

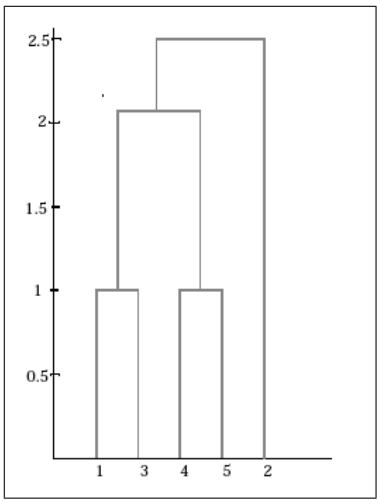

Figure 4.1 Form of hierarchical cluster tree (Dendrogram view). Horizontal axis is pairs of data set. Vertical axis is proximity of pairs.

There is also another advantage of calculating time frames' resemblances and grouping temporally consecutive scalp maps with similar topologies; by this way during one main topology's lasting period, complexity and variety of all scalp map series is decreased and making decision about results of spatial analysis is getting easier.

To perform hierarchical cluster analysis on our data set, this standard procedure was followed:

- Finding the similarity or dissimilarity between every time frame in the data set.
- Grouping the time frames into a binary, hierarchical cluster tree.
- Determining main clusters of hierarchical cluster tree.

4.1.1 Finding the Similarity or Dissimilarity Between Every Time Frame in the Data Set

In this step, the distances between time frames are calculated using a pair wise distance function in written Clustering Toolbox (Figure 4.2). This function supports

six different ways to compute distance measurement. These are Euclidean Distance, Standardized Euclidean Distance, Mahalanobis Distance, City Block Metric, Cosine Distance, Correlation Distance. We applied all these distance measurement ways for our data because we haven't got any prediction about their success while concerning scalp map clustering.

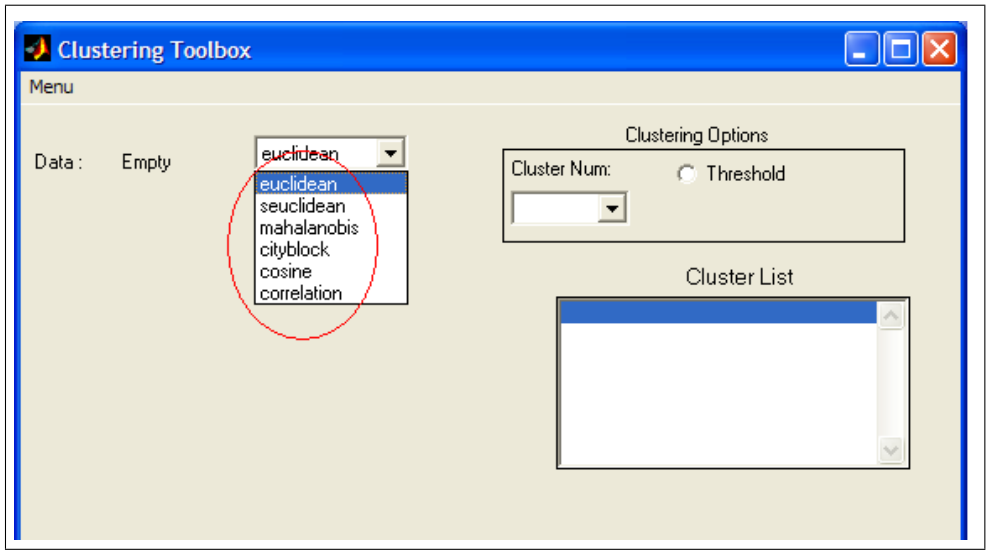

Figure 4.2 Distance measurement options in Clustering Toolbox. Appendix B

Each time frame has 30 recording points on scalp. During the analysis 100 time frames are taken from post stimulus period of averaged target set recording of 18 subjects. Now, we have a 100-by-30 data matrix X, which is treated as 100 (1-by-30) row vectors (time frames) x_1, x_2, ..., x_{100} the various distances between the vector x_r and x_s are defined as follows:

Euclidean distance:

$$d_{rs}^2 = (x_r - x_s)(x_r - x_s)' \tag{4.1}$$

Standardized Euclidean distance:

$$d_{rs}^2 = (x_r - x_s)D^{-1}(x_r - x_s)' \tag{4.2}$$

where, D is the diagonal matrix with diagonal elements given by v_j^2 (Eq. 4.3), which

denotes the variance of the variable X_j over the m objects.

$$\upsilon_j^2 = \sum_{i=1}^{m}(X_{(i,j)} - mean(X_{(:,j)}))^2/(m-1) \tag{4.3}$$

Mahalanobis distance:

$$d_{rs}^2 = (x_r - x_s)V^{-1}(x_r - x_s)' \tag{4.4}$$

where, V is the sample covariance matrix.

City Block metric:

$$d_{rs} = \sum_{j=1}^{n} |x_{rj} - x_{sj}| \tag{4.5}$$

Cosine distance:

$$d_{rs} = (1 - x_r x_s'/(x_r' x_r)^{\frac{1}{2}}(x_s' x_s)^{\frac{1}{2}}) \tag{4.6}$$

Correlation distance:

$$d_{rs} = 1 - \frac{(x_r - \overline{x}_r)(x_s - \overline{x}_s)'}{[(x_r - \overline{x}_r)(x_r - \overline{x}_r)']^{\frac{1}{2}}[(x_s - \overline{x}_s)(x_s - \overline{x}_s)']^{\frac{1}{2}}} \tag{4.7}$$

where, $\overline{x}_r = \frac{1}{n}\sum_j x_{rj}$ and $\overline{x}_s = \frac{1}{n}\sum_j x_{sj}$

Distances are arranged in the order $(1,2),(1,3),...,(1,m),(2,3),...,(2,m)...,(m-1,m)$. In this vector (i,j) means distance between time frames i and j. For a time frame data set made up of m time frames, there are $(m-1).m/2$ pairs at distance vector. This vector is also commonly known as a similarity matrix or dissimilarity matrix.

ERP time frames' pair wise distances are calculated and constructed distance vectors according to above-mentioned six different ways. In our case, m is equal to 100, so we have 4950 pairs at six different distance vectors.

4.1.2 Grouping the Time Frames into a Binary, Hierarchical Cluster Tree

In this step, pairs of ERP recordings that are in close proximity are linked using a linkage function. The linkage function uses the distance information generated in previous step to determine the proximity of time frames to each other. As time frames are paired into binary clusters, the newly formed clusters are grouped into larger clusters until a hierarchical tree is formed (Fig. 4.1).

There are different linking methods. Average linkage uses the average distance between all pairs of objects (Eq. 4.9). Ward linkage uses the incremental sum of squares; that is, the increase in the total within-group sum of squares as a result of joining groups (Eq. 4.10). Single linkage, also called nearest neighbor, uses the smallest distance between objects in the two groups. Complete linkage, also called furthest neighbor, uses the largest distance between objects in the two groups.

We used Cophenetic correlation coefficient (Eq. 4.8) in order to choose linking method. The Cophenet function measures the distortion of this classification, indicating how readily the data fits into the structure suggested by the classification.

$$c = \frac{\sum_{i<j}(Y_{ij} - y)(Z_{ij} - z)}{\sqrt{\sum_{i<j}(Y_{ij} - y)^2 \sum_{i<j}(Z_{ij} - z)^2}} \tag{4.8}$$

where, Y_{ij} is the distance between objects i and j in Y (generated by distance function),
Z_{ij} is the distance between objects i and j in Z (generated by linkage function),
y is the average value of Y,
z is the average value of Z.

The magnitude of Cophenetic correlation coefficient should be very close to 1 for a high-quality solution. Cophenetic correlation coefficients for each distance measurement way and linking method couples are presented in Table 4.1. Results show that we must use Ward linking method for Mahalanobis distance and Average linking method for remaining distant calculation ways.

Table 4.1
The Cophenetic correlation coefficients of linking methods for each distance measurement techniques.

	Average	Ward	Complete	Single
Euclidean distance	0.8335	0.8079	0.8302	0.6570
Standardized Euclidean distance	0.8222	0.7970	0.8119	0.6891
Mahalanobis distance	0.6387	0.8051	0.6186	0.5547
City Block metric	0.8209	0.8001	0.8104	0.6593
Cosine distance	0.9054	0.8537	0.8142	0.7836
Correlation Distance	0.8361	0.7641	0.8230	0.7330

In cluster r and cluster s, Average linkage calculation is made during the formation of cluster tree as follows:

$$d(r,s) = \frac{1}{n_r}\frac{1}{n_s}\sum_{i=1}^{n_r}\sum_{j=1}^{n_s} dist(n_{ri}, n_{sj}) \tag{4.9}$$

where, n_r and n_s are number of objects in cluster r and cluster s respectively. n_{ri} is the i^{th} object in cluster r. n_{sj} is the j^{th} object in cluster s.

Ward linkage is given by:

$$d(r,s) = n_r n_s d_{rs}^2/(n_r + n_s) \tag{4.10}$$

where, d_{rs}^2 is the distance between cluster r and cluster s.

After linking process, we have six hierarchical cluster trees made by six distance measurement techniques and selected linkage method.

4.1.3 Determining Main Clusters of Hierarchical Cluster Tree

Last step of hierarchical cluster analysis is to determine main clusters. One option is to select a threshold for cutting cluster tree into clusters. Clusters are formed when proximity values of pairs are less than selected threshold value.

In our case however, we have no prediction about threshold and we used another option which is to predefine the number of clusters. We decided to detect six main clusters from six different dendrograms of 500 ms post-stimulus part of recordings (100 time frames). But, predefining the number of clusters couldn't satisfy our clustering criterion which is, clusters have to include consecutive time frames. Beside that, high variety of scalp topologies especially during the very early period of recordings produced clusters constituted by one or two frames. Actually this is an expected result if we consider rapid changes of scalp topologies during that period. In addition, there is not a standard variation between the members of each cluster. In other words, scalp topology variance within a cluster is not same with the other clusters. These reasons were close us to select clusters from dendrograms by manually.

We selected six branches from six dendrograms which include maximum number of consecutive time frames and neglect clusters with one or two members and reject members with high inconsistent scalp map topologies with the nearest neighbor. Dendrogram plots (Figures 4.3, 4.6, 4.9, 4.12, 4.15, 4.18) of clusters, time window placements of clusters (Figures 4.4, 4.7, 4.10, 4.13, 4.16, 4.19), and average topological scalp maps of each clusters (Figures 4.5, 4.8, 4.11, 4.14, 4.17, 4.20) were plotted.

Euclidean distance clustering results are given in Figures 4.3 - 4.5.

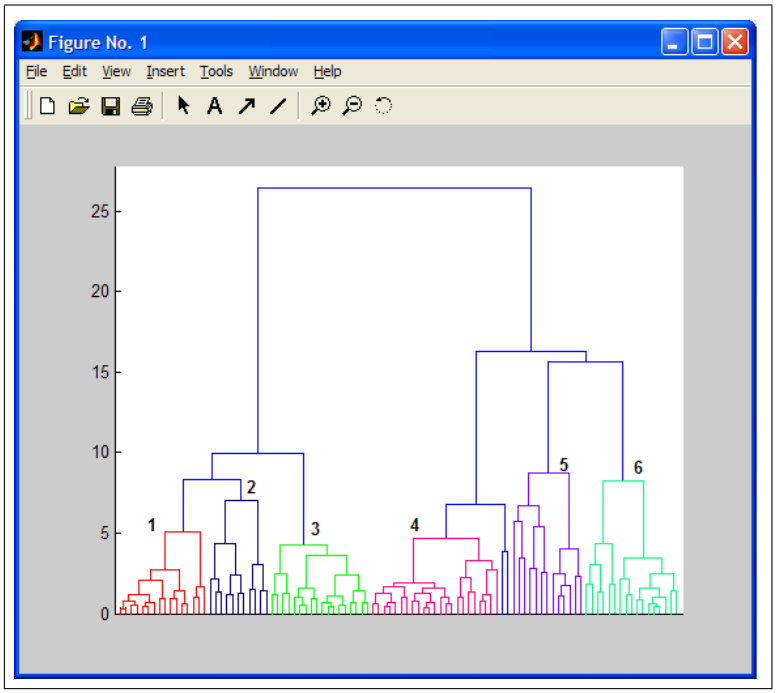

Figure 4.3 Dendrogram view and selected six clusters based on Euclidean distance.

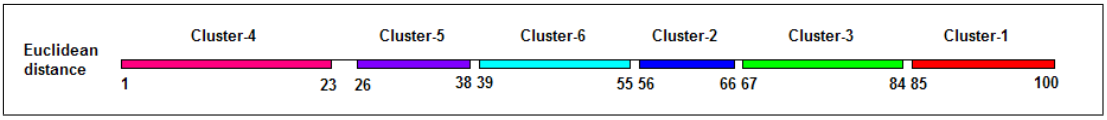

Figure 4.4 Time window placements of selected clusters based on Euclidean distance.

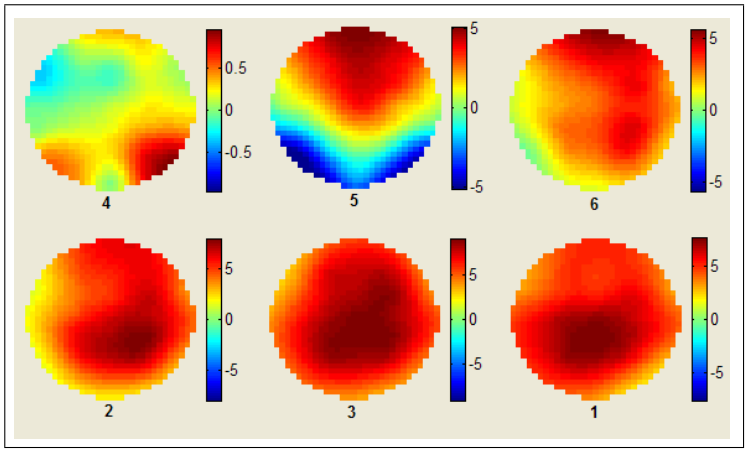

Figure 4.5 Average scalp map plots of selected clusters based on Euclidean distance.

S. Euclidean distance clustering results are given in Figures 4.6 - 4.8.

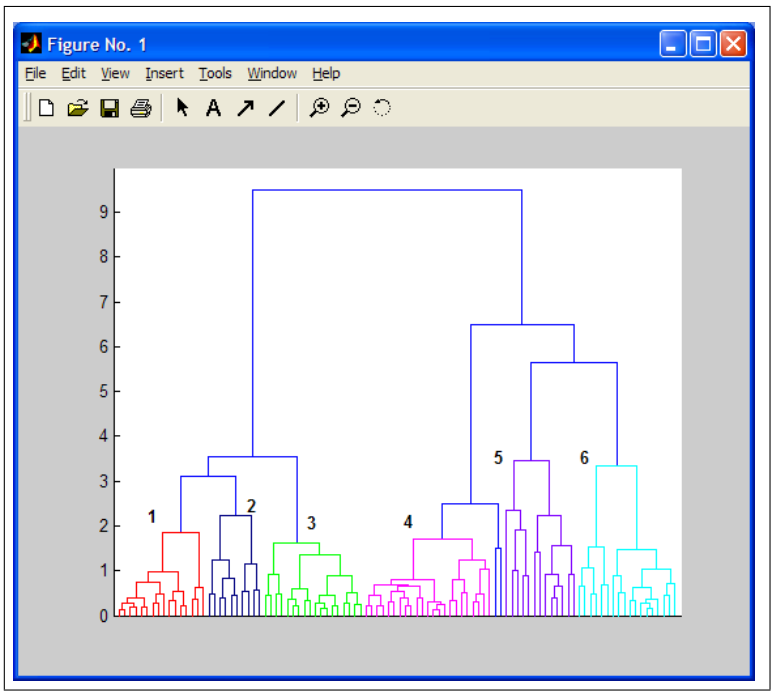

Figure 4.6 Dendrogram view and selected six clusters based on S. Euclidean distance.

Figure 4.7 Time window placements of selected clusters based on S. Euclidean distance.

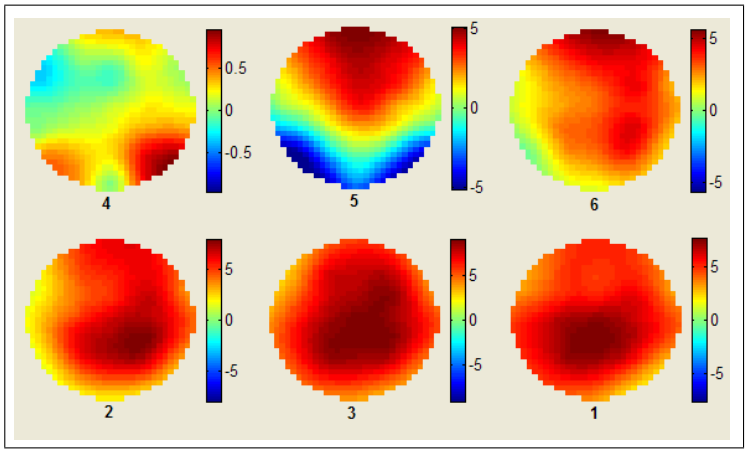

Figure 4.8 Average scalp map plots of selected clusters based on S. Euclidean distance.

Mahalanobis distance clustering results are given in Figures 4.9 - 4.11.

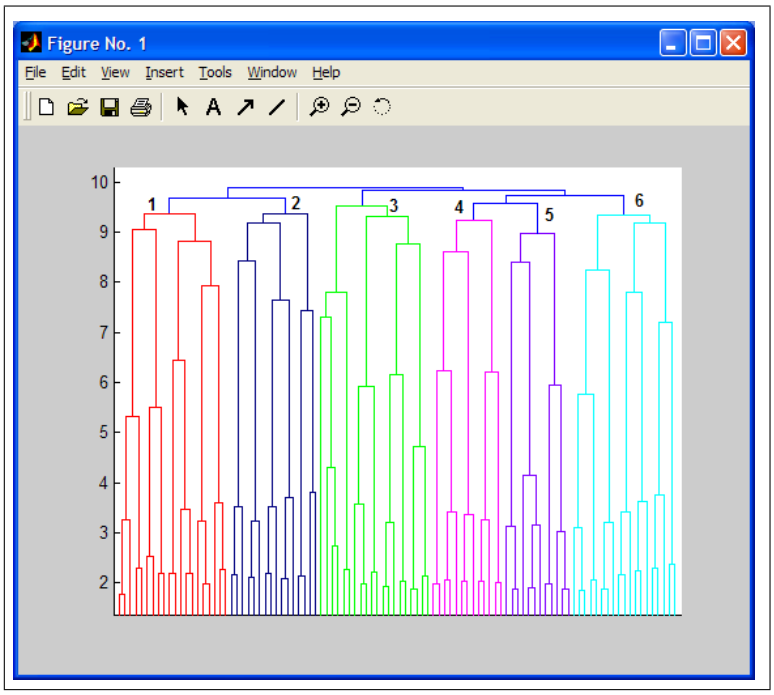

Figure 4.9 Dendrogram view and selected six clusters based on Mahalanobis distance.

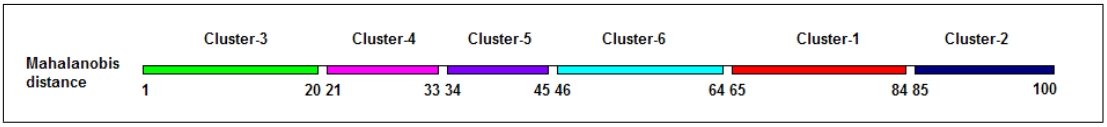

Figure 4.10 Time window placements of selected clusters based on Mahalanobis distance.

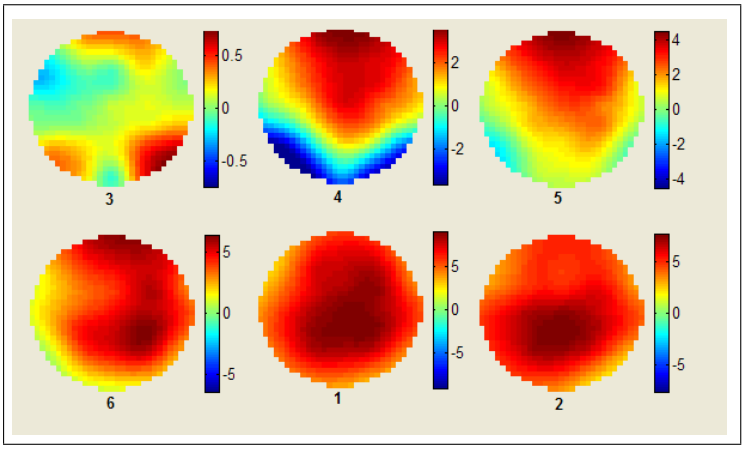

Figure 4.11 Average scalp map plots of selected clusters based on Mahalanobis distance.

City Block metric clustering results are given in Figures 4.12 - 4.14.

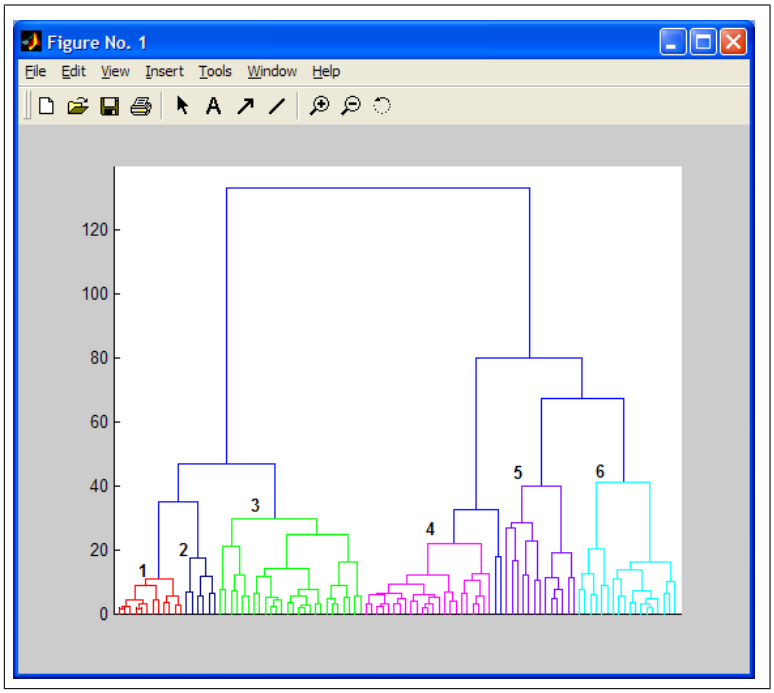

Figure 4.12 Dendrogram view and selected six clusters based on City Block metric.

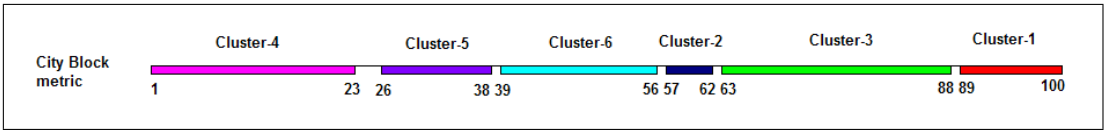

Figure 4.13 Time window placements of selected clusters based on City Block metric.

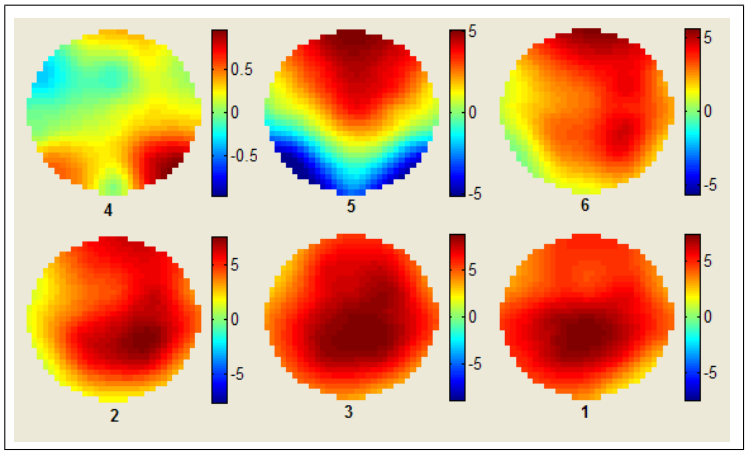

Figure 4.14 Average scalp map plots of selected clusters based on City Block metric.

Cosine distance clustering results are given in Figures 4.15 - 4.17.

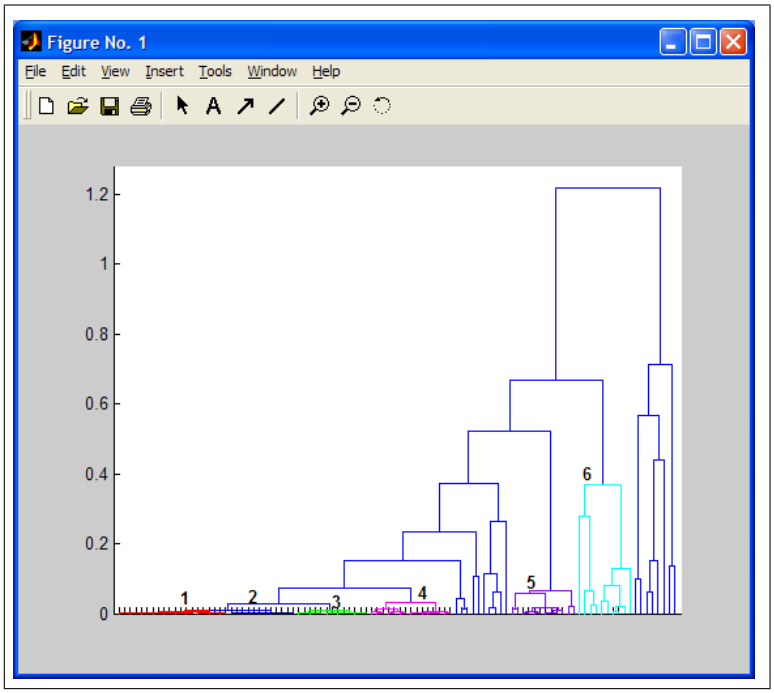

Figure 4.15 Dendrogram view and selected six clusters based on Cosine distance.

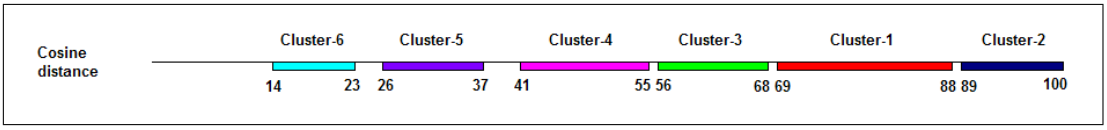

Figure 4.16 Time window placements of selected clusters based on Cosine distance.

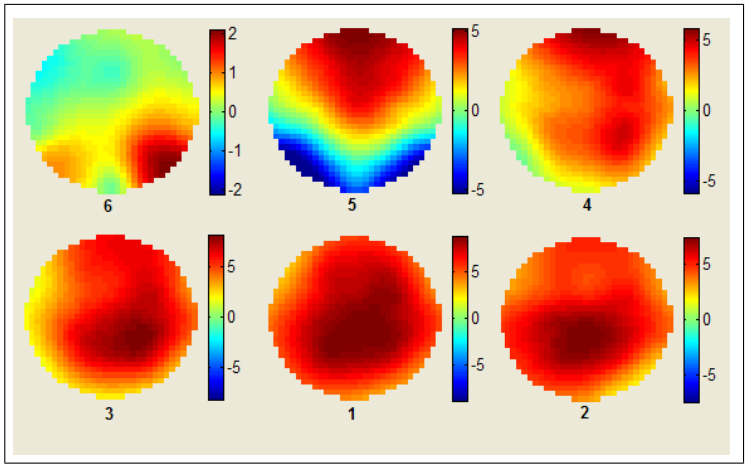

Figure 4.17 Average scalp map plots of selected clusters based on Cosine distance.

Correlation distance clustering results are given in Figures 4.18 - 4.20.

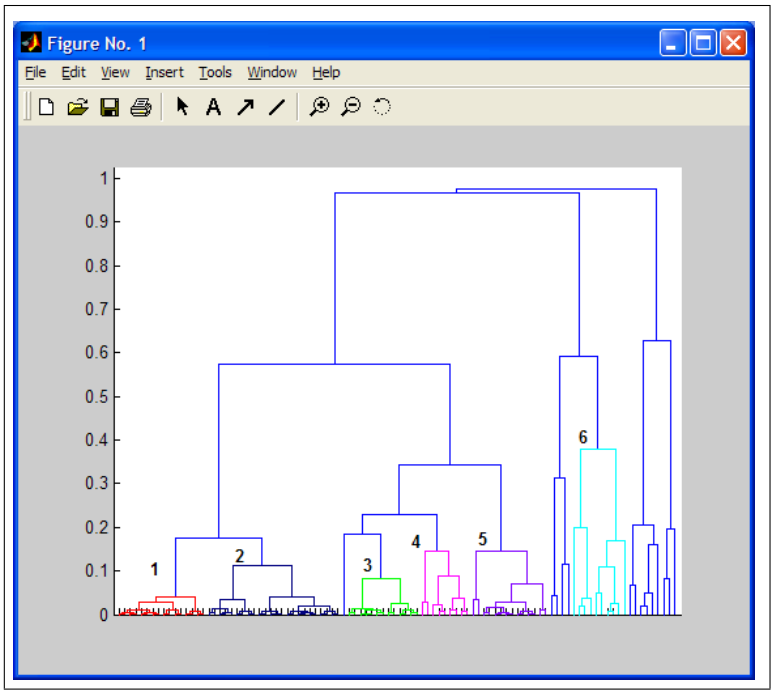

Figure 4.18 Dendrogram view and selected six clusters based on Correlation distance.

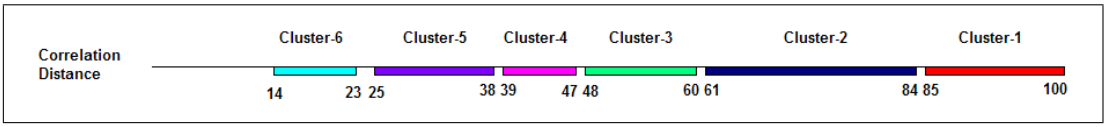

Figure 4.19 Time window placements of selected clusters based on Correlation distance.

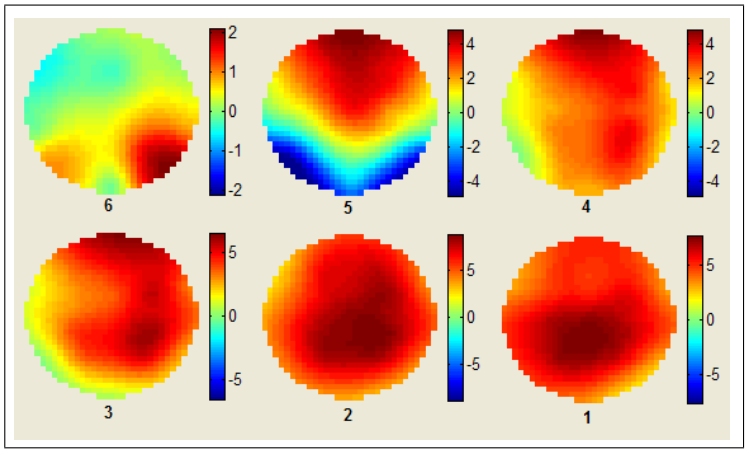

Figure 4.20 Average scalp map plots of selected clusters based on Correlation distance.

As can be seen from the average scalp map plots of selected clusters for each distance measurement technique, there is a high resemblance between topologies. Average scalp maps of first, second, fifth and sixth time windows have nearly the same topology. Difference between the average scalp maps results is obvious but not very far at third and fourth time windows.

Because of this high similarity, we could not separate one of the distance measurement technique and talk about its superiority to other techniques. Moreover, all these techniques have scientific validity in certain application areas. That's why, we selected clustering technique based on their linking success instead of their performance. Linking success was calculated by Cophenetic correlation function. Average linking of Cosine distance measurement technique results was chosen because it gave the lowest distortion at classification (Table 4.1).

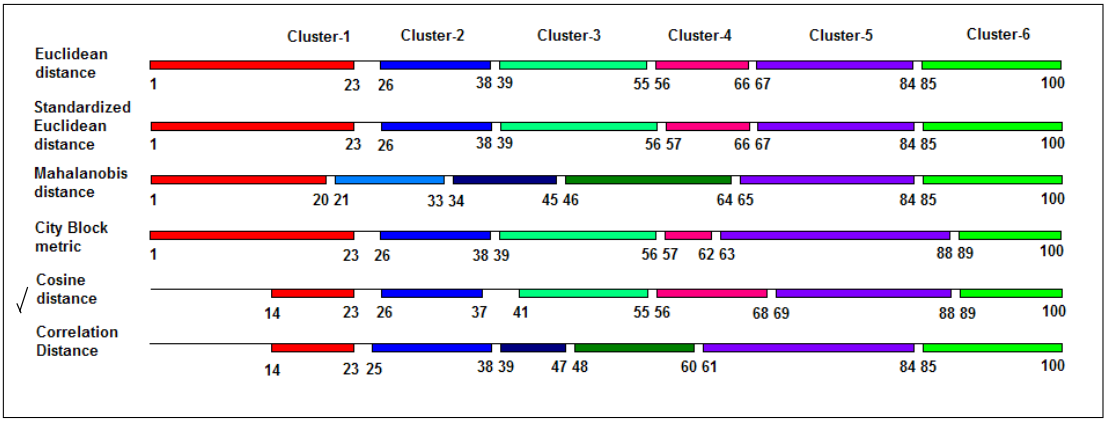

Figure 4.21 Forming clusters from different distance calculation ways by pre-defining cluster number.

4.2 Spatial Wavelet Analysis

The two dimensional wavelet decomposition of interpolated time frames produces four wavelet coefficients (one approximation and three details) for each octave, as described in Chapter 2. Since, wavelet analysis satisfies multiresolution requirements, it is possible to combine the decomposition results for different purposes. We

will reconstruct detail coefficients (horizontal, vertical, diagonal details) together at each level because we need one detail image includes all detail information. That is, after decomposition step, approximation coefficient and detail coefficients are used to reconstruct two images (approximation, detail) rather than four images [16].

The discrete wavelet decomposition starts from finest level. After decomposition, approximation coefficients are decomposed to get the approximation and detail coefficients at the next level. Because of the dyadic structure of wavelet decomposition, there is a limit on how many levels (octaves) wavelet decomposition can be applied. In our case, size of the scalp maps are 32 by 32 points (2^5 by 2^5), and we apply 4 octave wavelet analysis.

Another consideration is how to choose a proper wavelet for such multiresolution analysis. Many wavelet families have been constructed in the literature. The idea is that a less smooth wavelet should be chosen if the image is rough, and a smoother wavelet should be chosen if the image is smooth. If one chooses a smooth wavelet for a rough image, one would not see some details because they are smoothed out. On the other hand, if one chooses a rough wavelet for a smooth image, one could create some artificial bumps. We used the Wavelet Analyzing Toolbox with user interface written in MATLAB in order to choose wavelet type and order (Appendix A).

4.2.1 Choice of Wavelet Type

In the working memory paradigm used to generate the present data, a right hemispheric activation is expected in the beginning of the memory search process, which however cannot be observed clearly in the raw ERP topography. That's why; we have initially selected one interpolated time frame (215 ms) where this specific neuro-anatomical pattern was expected (Figure 4.23).

Decomposition of the raw topography into distinct focal patterns in different scales is the main feature in choosing the optimum spatial filter. Different wavelet

types and orders in the written Wavelet Analyzing Toolbox was applied. Discrete Meyer Wavelet could dissociate a right fronto-parietal activation(see Figure 4.23) which fits to the expectations for this time frame (215 ms) of the Sternberg Paradigm according to our functional neuro-anatomical knowledge.

Discrete Meyer Wavelet [17], which is the FIR based approximation of the Meyer wavelet[18] was chosen (see Figure 4.22).

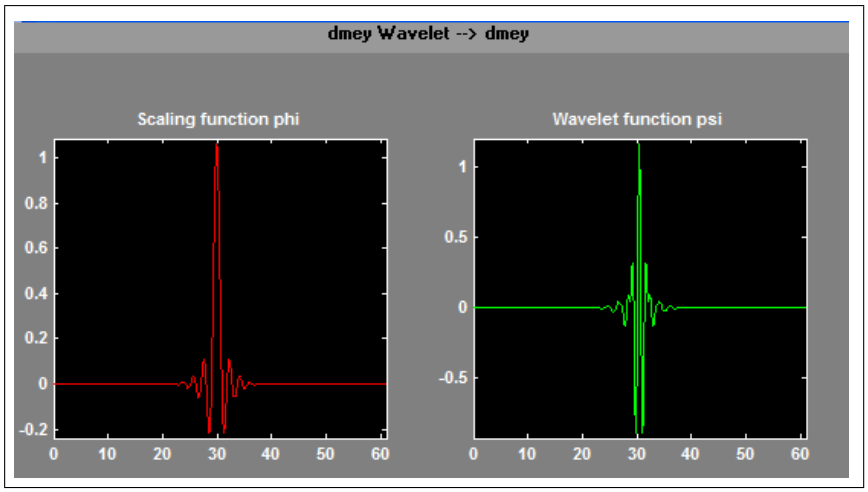

Figure 4.22 Discrete Meyer scaling and wavelet functions.

Discrete Meyer Wavelet has the following features:

- Orthogonal, Biorthogonal → yes
- Compact support→ yes
- DWT, CWT→ possible

Decomposition and reconstruction results are presented in Figure 4.23. In this Figure, approximation coefficients, reconstructed approximation maps and reconstructed detail maps for 4 octaves are shown. First octave detail map shows the highest spatial components that were separated which is nearly zero (left bottom). First octave approximation map shows what remains after separation of first octave detail map

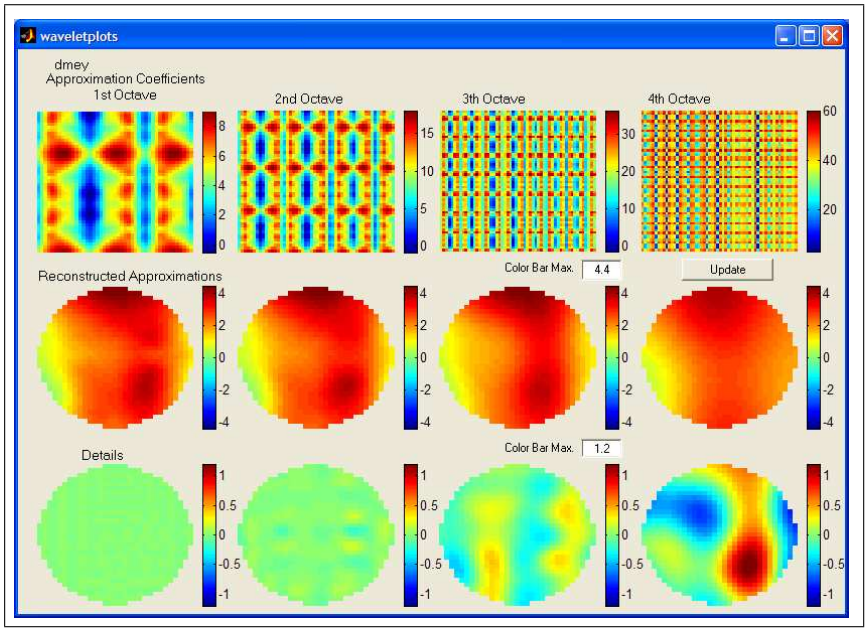

Figure 4.23 Decomposed and reconstructed time frame (at 215 ms) by discrete Meyer wavelet.

from raw map. Second octave approximation map shows what remains after first and second octave detail maps were separated.

All detail maps and 4th octave approximation map contain enough information for raw map. However, we will calculate just 4th octave approximation and detail maps for future analysis, because they contain main properties of raw map. This also means, we will show and use two maps (4th octave detail and 4th octave approximation maps) as the results of spatial wavelet analysis for each scalp map, keeping in mind that these two maps can not fully represent raw scalp map.

4.2.2 Spatial Wavelet Analysis Results of Main Topologies

After selecting proper wavelet type, spatial wavelet analysis is applied for six clusters, detected by hierarchical cluster analysis. Brain maps and their reconstructed approximation and detail maps are shown in Figure 4.24 - 4.29.

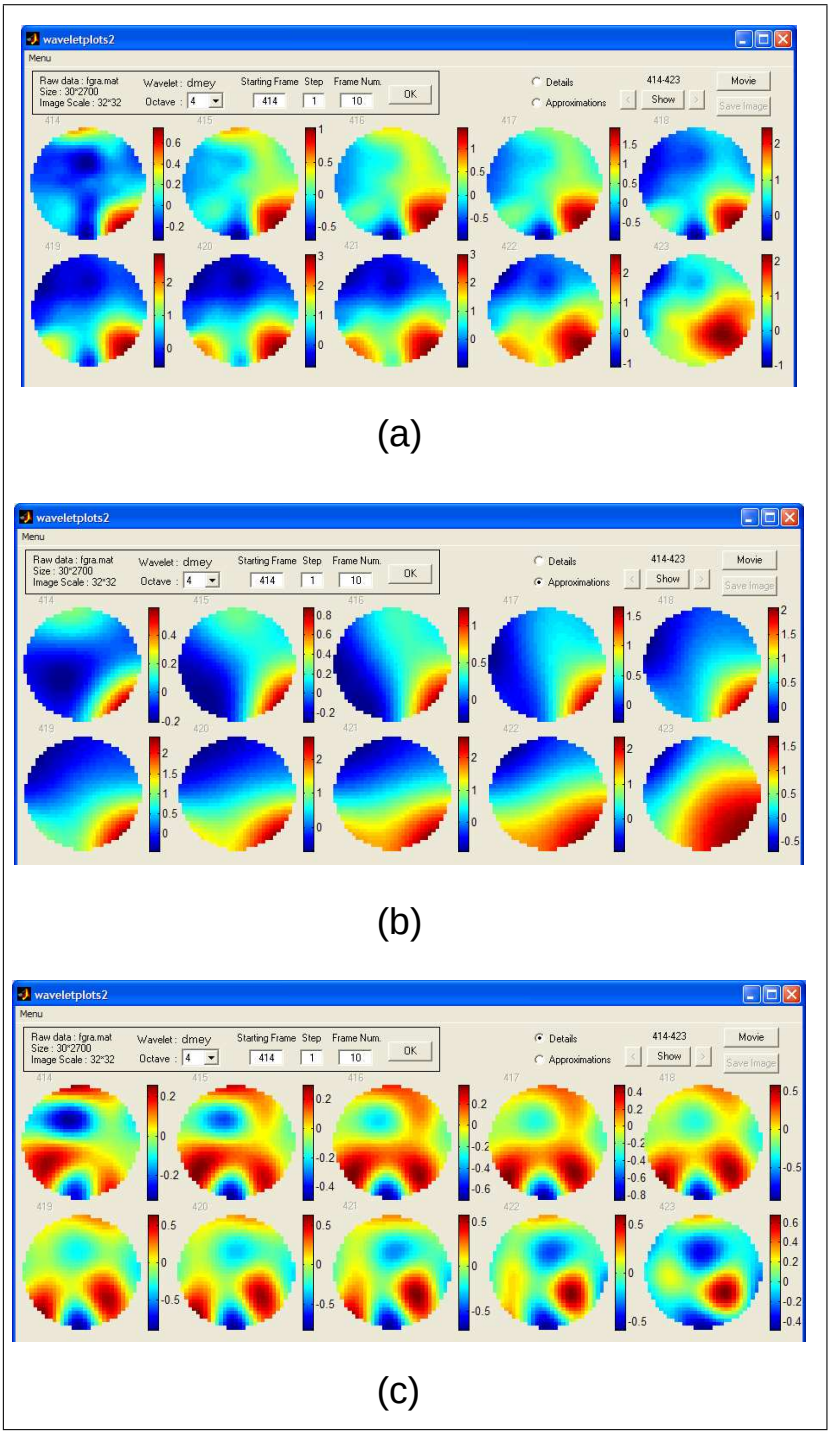

Figure 4.24 (a) Interpolated time frames, (b) Reconstructed approximation maps, (c) Reconstructed detail maps of cluster 1 (70-115 ms).

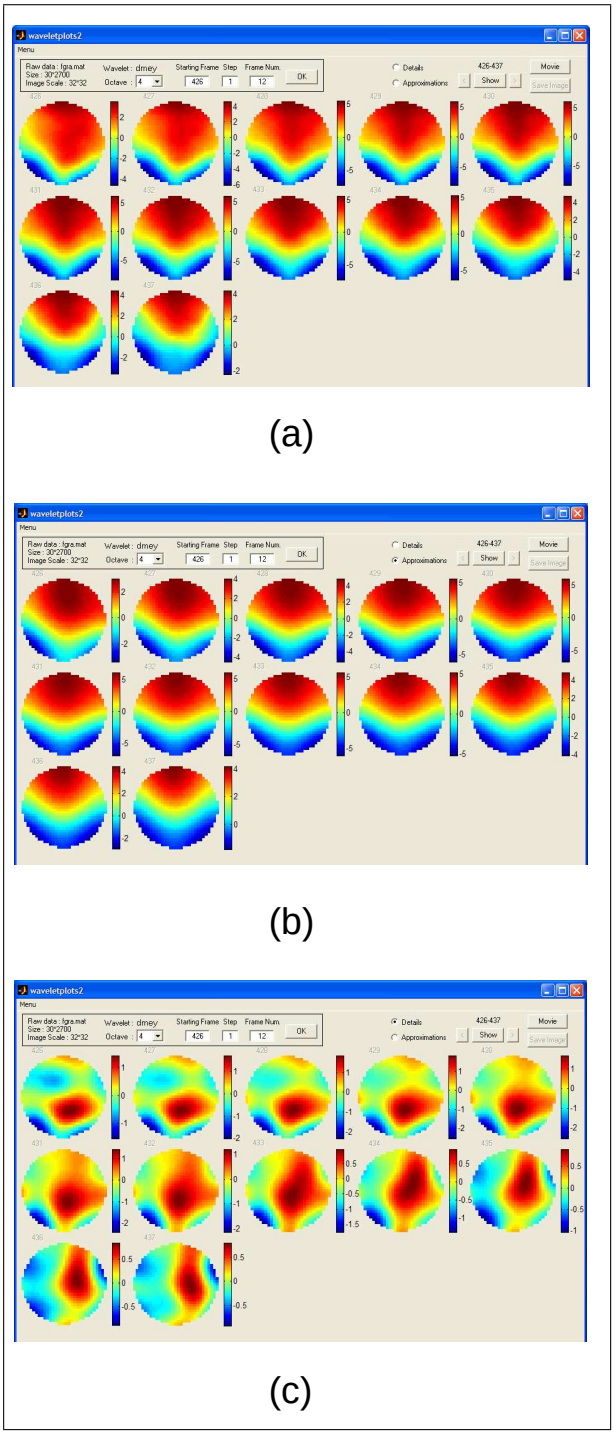

Figure 4.25 (a) Interpolated time frames, (b) Reconstructed approximation maps, (c) Reconstructed detail maps of cluster 2 (130-185 ms).

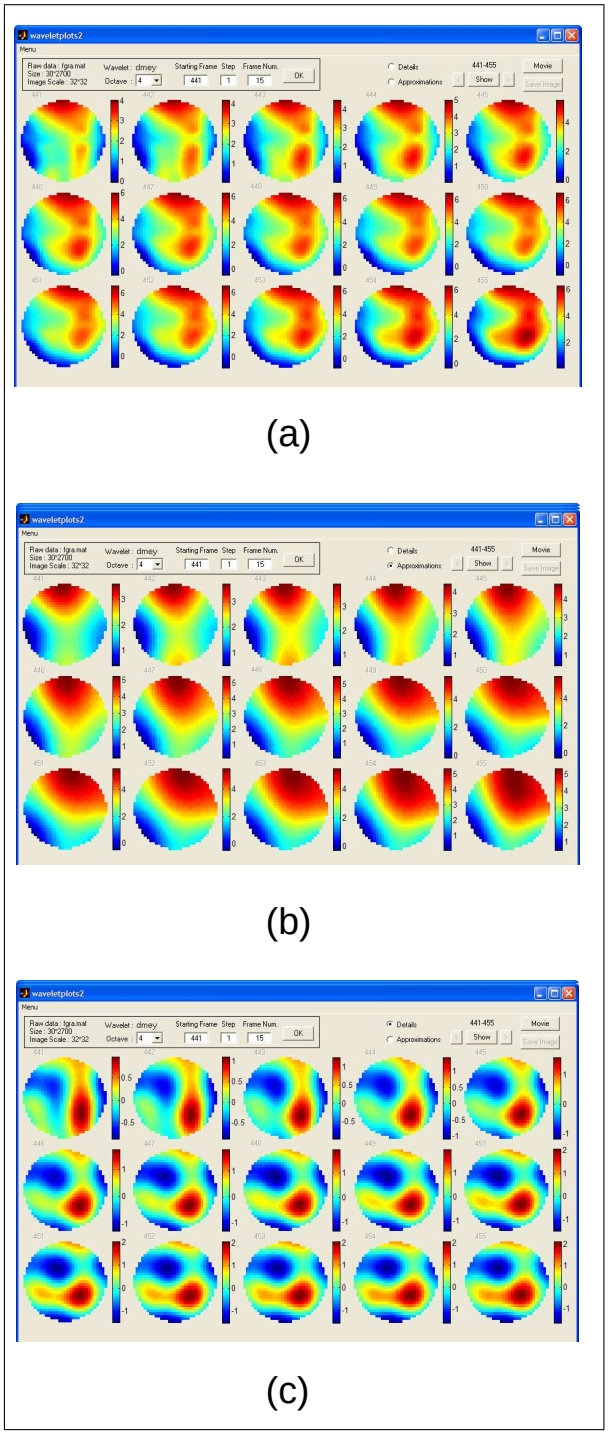

Figure 4.26 (a) Interpolated time frames, (b) Reconstructed approximation maps, (c) Reconstructed detail maps of cluster 3 (205-275 ms).

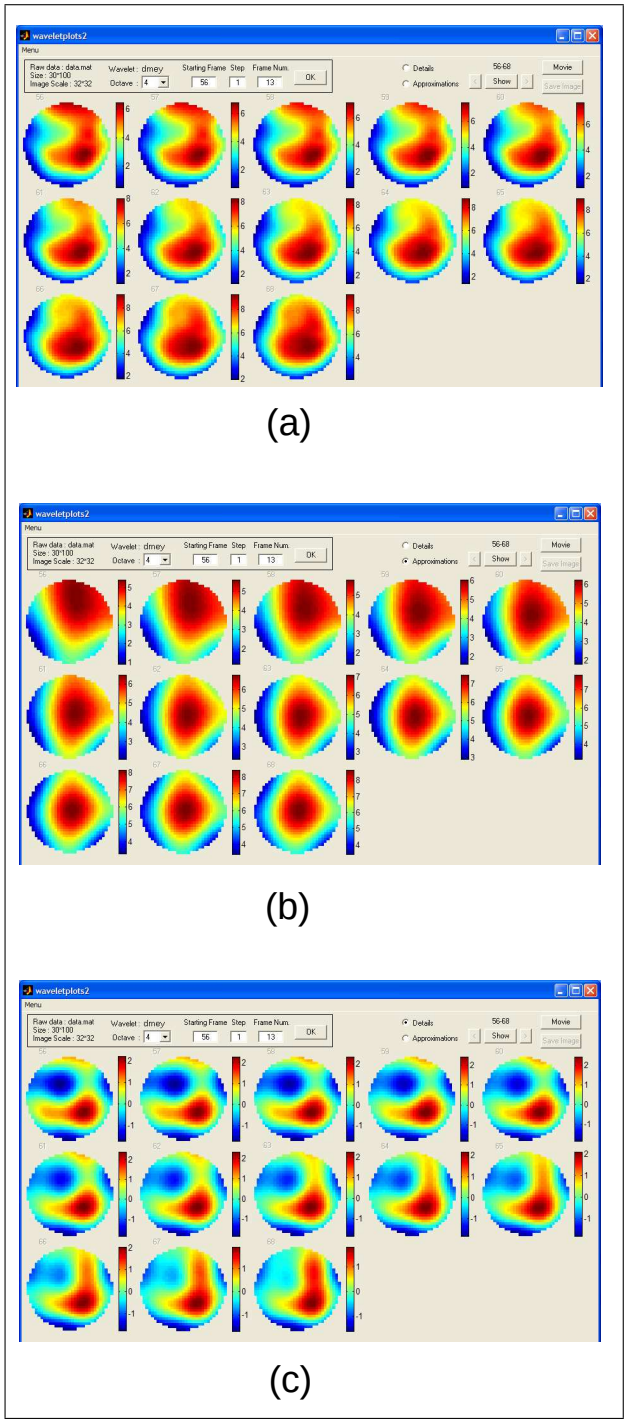

Figure 4.27 (a) Interpolated time frames, (b) Reconstructed approximation maps, (c) Reconstructed detail maps of cluster 4 (280-340 ms).

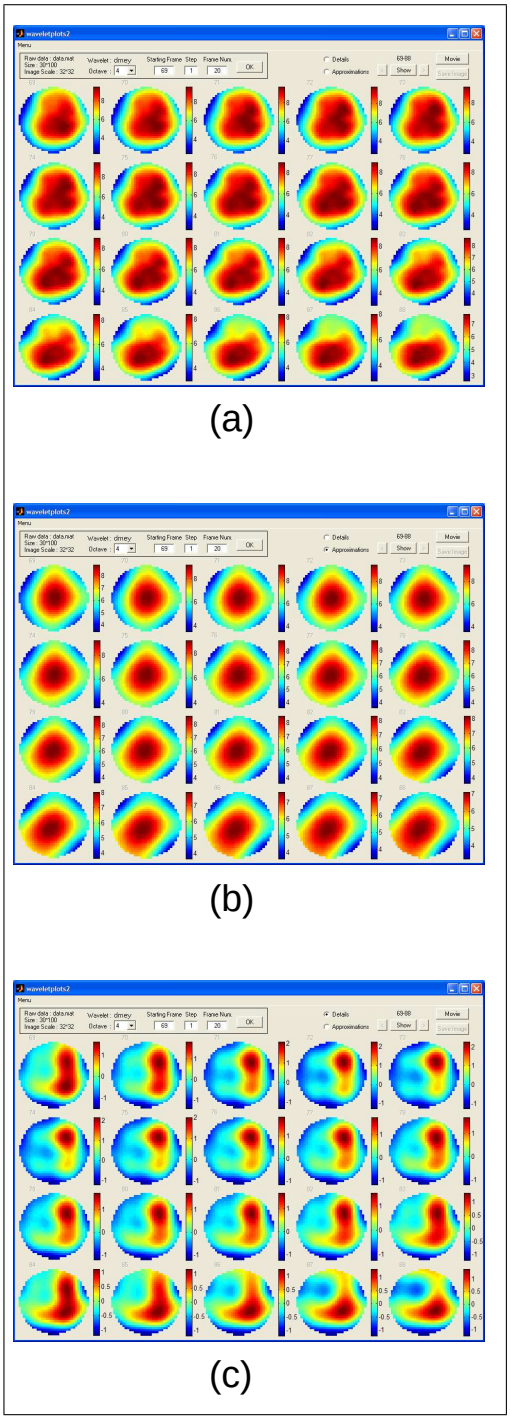

Figure 4.28 (a) Interpolated time frames, (b) Reconstructed approximation maps, (c) Reconstructed detail maps of cluster 5 (345-440 ms).

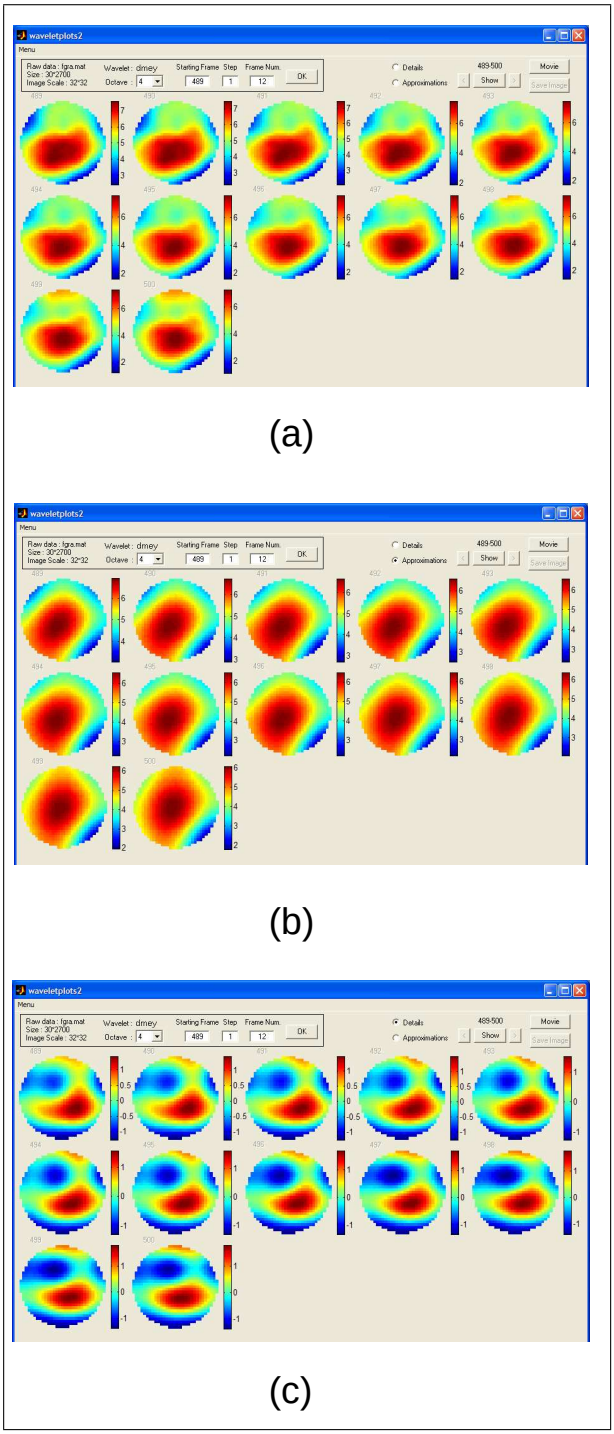

Figure 4.29 (a) Interpolated time frames, (b) Reconstructed approximation maps, (c) Reconstructed detail maps of cluster 6 (445-500 ms).

5. LORETA APPLICATION

5.1 Low Resolution Electromagnetic Tomography (LORETA)

From the scalp-recorded electrical potential distribution, LORETA computes the 3-D intracerebral distributions of current density for specified EEG frequency bands [9], [19], [20]. LORETA makes three major assumptions in estimating the source location of electrical activity: (1) that adjacent neurons act in synchrony, so that the activation distribution can be modelled as a smoothly varying field; (2) that the smoothest activity distribution is the most plausible; and (3) that the signal measured at the brain surface does not emanate from white matter or from certain subcortical structures deep in the brain.

Because of that we did not focus on inverse problem methods or details in this work, formulations and other theoretical background of LORETA haven't presented here. Detailed information can be found at references [9], [19], [20].

5.2 Current Density Estimation of Spatial Wavelet Analysis Results

After obtaining the clustering and spatial wavelet analysis results in Chapter 4, we apply an inverse transform from scalp maps to scalp electrode potentials. We build up an ERP recording sequence. In this sequence, there are three parts for six clusters. These parts include raw, detail, and approximation ERP recordings. First cluster includes 10 raw, 10 detail, and 10 approximation time frames. Final sequence includes totally 246 time frames (First cluster: 3x10 + Second cluster: 3x12 + Third cluster: 3x15 + Fourth Cluster: 3x13 + Fifth cluster: 3x20 + Sixth cluster: 3x12 time frames).

We used above-mentioned ERP recording sequence, electrode locations (see Figure 3.2) and LORETA transformation matrix produced from electrode locations in converting ERP recordings to LORETA images by using LORETA Toolbox [21]. We used average neuronal generator distribution option for each LORETA images which are presented in Figure 5.1 - 5.11. Each Figure (Figure 5.1 - 5.11) includes 3 image parts (a, b, c). Image (a) indicates current density estimation of raw ERP recordings (local maxima). Image (b) and (c) indicate current density estimations of ERP sequences, which were produced from spatial low and high frequency components of raw scalp maps, respectively. All images show 3 orthogonal slices through the brain. Typically, anatomy is presented in greys. Positive LORETA values in red, zero in white. In the image, left slice is axial (horizontal), viewing the head from top. L = Left, R = Right. The center slice is saggital, view from the left. A = Anterior, P = Posterior. The right slice is coronal, viewed from the back. All axes and specified coordinates are in Talairach space.

There are also tables, following images (Table 5.2 - 5.12). These tables include coordinates and locations of maximum activation points in the brain. These points are; top 3 activation points of raw ERP sequence on the left, and local maxima of separated approximation (spatial low frequency component) and detail (spatial high frequency component) on the right.

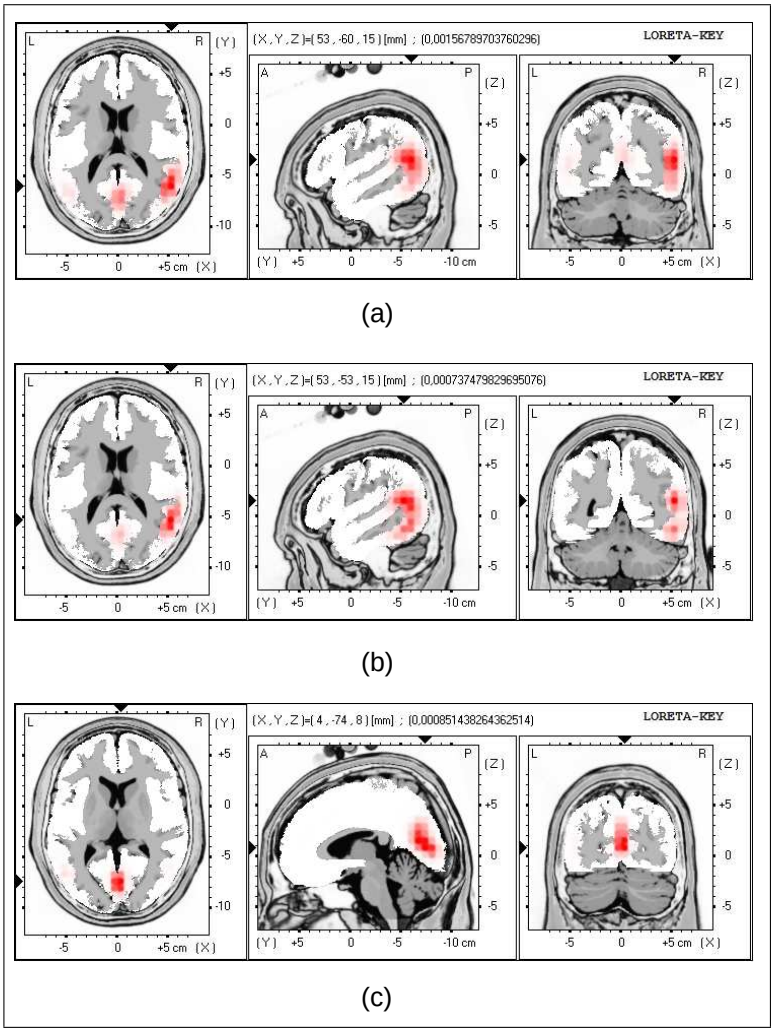

Figure 5.1 LORETA results of (a) raw ERP sequence, and sequences produced from (b) approximation (low spatial frequency) component, (c) detail (low spatial frequency) component of scalp maps of Cluster-1 (70-115 ms).

	TX	TY	TZ								
Raw	53	-60	15	Temporal Lobe	Superior Temporal Gyrus	⇨	Approximation	53	-53	15	Temporal Lobe	Superior Temporal Gyrus
	4	-74	8	Occipital Lobe	Cuneus	⇨	Detail	4	-74	8	Occipital Lobe	Cuneus
	4	-81	8	Occipital Lobe	Cuneus							

Separated

Figure 5.2 Locations of three max. activations of raw ERP and its two separated components in Cluster-1.

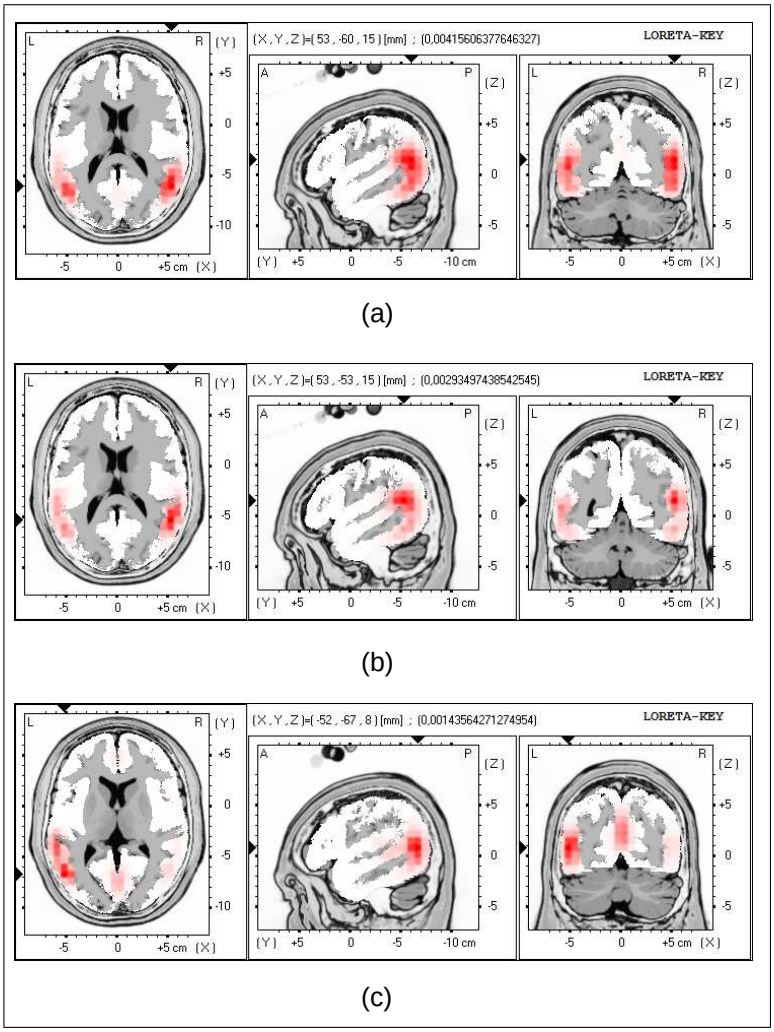

Figure 5.3 LORETA results of (a) raw ERP sequence, and sequences produced from (b) approximation (low spatial frequency) component, (c) detail (low spatial frequency) component of scalp maps of Cluster-2 (130-185 ms).

	TX	TY	TZ				Separated	TX	TY	TZ		
Raw	53	-60	15	Temporal Lobe	Superior Temporal Gyrus	⇨	Approximation	53	-53	15	Temporal Lobe	Superior Temporal Gyrus
	-52	-67	8	Temporal Lobe	Middle Temporal Gyrus	⇨	Detail	-52	-67	8	Temporal Lobe	Middle Temporal Gyrus
	53	-60	-6	Occipital Lobe	Middle Occipital Gyrus							

Figure 5.4 Locations of three max. activations of raw ERP and its two separated components in Cluster-2.

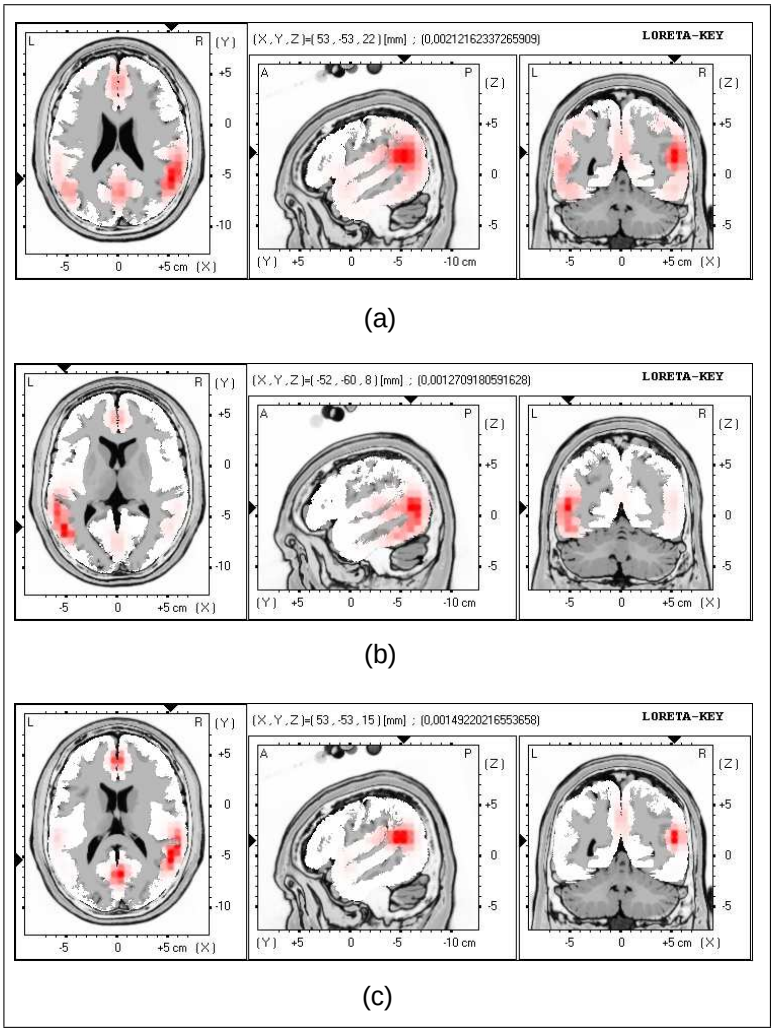

Figure 5.5 LORETA results of (a) raw ERP sequence, and sequences produced from (b) approximation (low spatial frequency) component, (c) detail (low spatial frequency) component of scalp maps of Cluster-3 (205-275 ms).

	TX	TY	TZ				TX	TY	TZ		
Raw	53	-53	22	Temporal Lobe	Inferior Parietal Lobule	⇨ Detail	53	-53	15	Temporal Lobe	Superior Temporal Gyrus
	-3	45	-6	Frontal Lobe	Medial Frontal Gyrus						
	-52	-60	8	Temporal Lobe	Middle Temporal Gyrus	⇨ Approximation	-52	-60	8	Temporal Lobe	Middle Temporal Gyrus

Separated

Figure 5.6 Locations of three max. activations of raw ERP and its two separated components in Cluster-3.

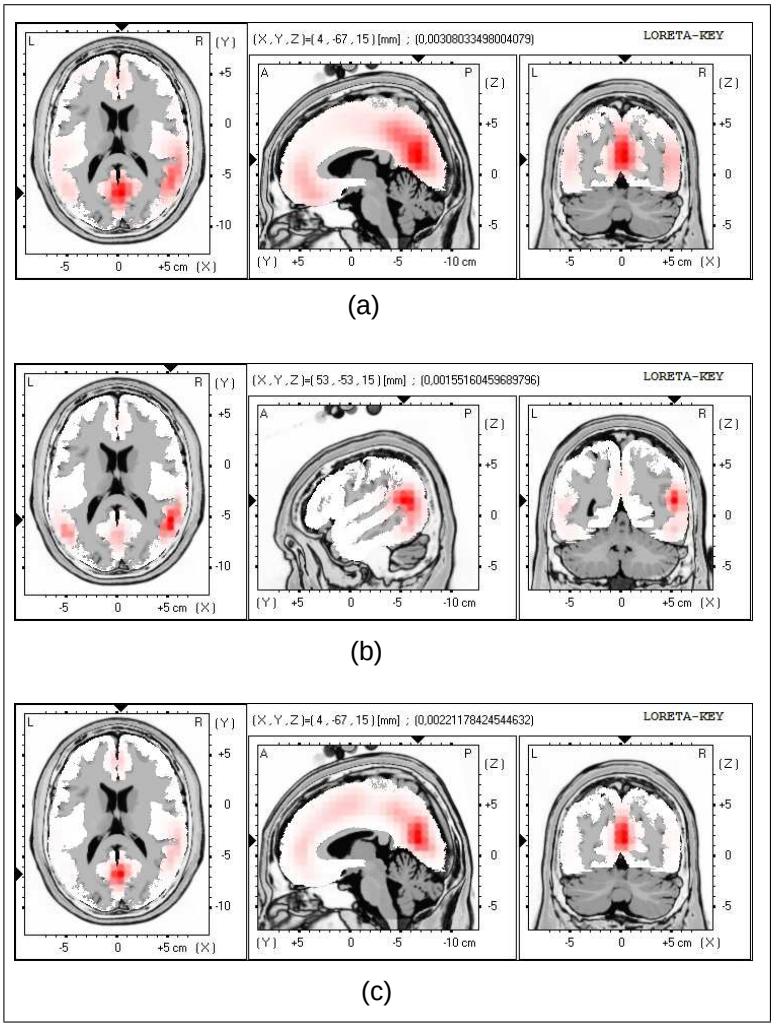

Figure 5.7 LORETA results of (a) raw ERP sequence, and sequences produced from (b) approximation (low spatial frequency) component, (c) detail (low spatial frequency) component of scalp maps of Cluster-4 (280-340 ms).

	TX	TY	TZ				Separated	TX	TY	TZ		
Raw	4	-67	15	Limbic Lobe	Posterior Cingulate	⇨	Detail	4	-67	15	Limbic Lobe	Posterior Cingulate
	53	-53	15	Temporal Lobe	Superior Temporal Gyrus	⇨	Approximation	53	-53	15	Temporal Lobe	Superior Temporal Gyrus
	-3	38	-20	Frontal Lobe	Medial Frontal Gyrus							

Figure 5.8 Locations of three max. activations of raw ERP and its two separated components in Cluster-4.

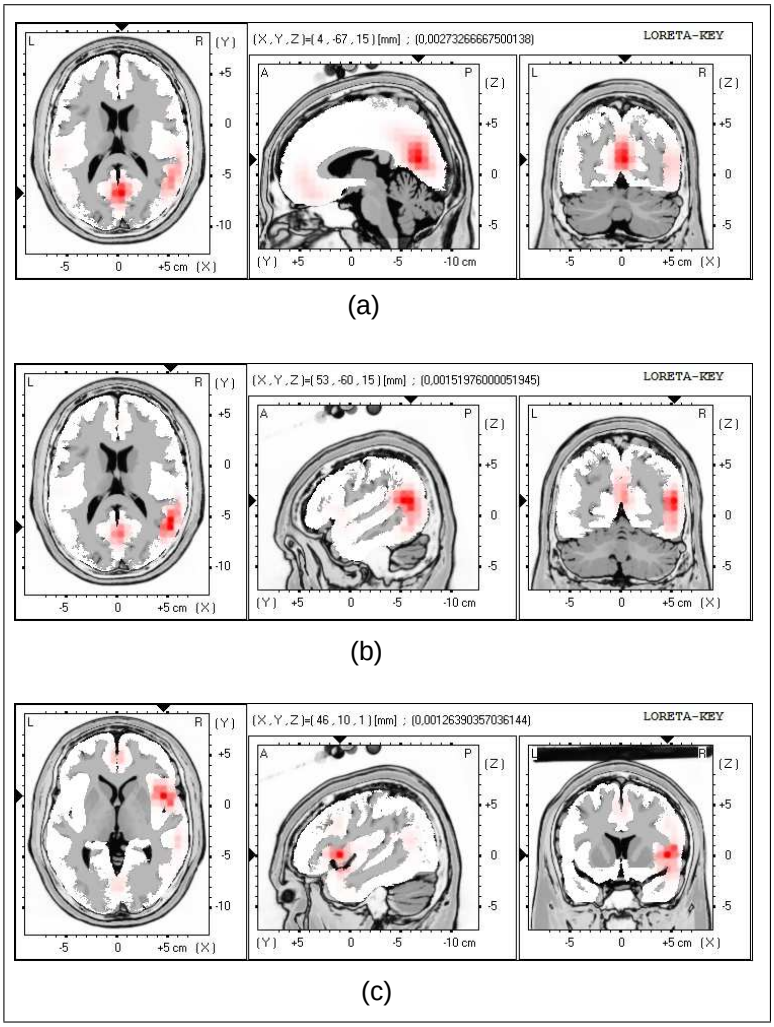

Figure 5.9 LORETA results of (a) raw ERP sequence, and sequences produced from (b) approximation (low spatial frequency) component, (c) detail (low spatial frequency) component of scalp maps of Cluster-5 (345-440 ms).

	TX	TY	TZ		
Raw	4	-67	15	Limbic Lobe	Posterior Cingulate
	53	-53	15	Temporal Lobe	Superior Temporal Gyrus
	-3	38	-20	Frontal Lobe	Medial Frontal Gyrus

⇨

Separated	TX	TY	TZ		
Detail	46	10	1	Insula	Sublobar
Approximation	53	-60	15	Temporal Lobe	Superior Temporal Gyrus

Figure 5.10 Locations of three max. activations of raw ERP and its two separated components in Cluster-5.

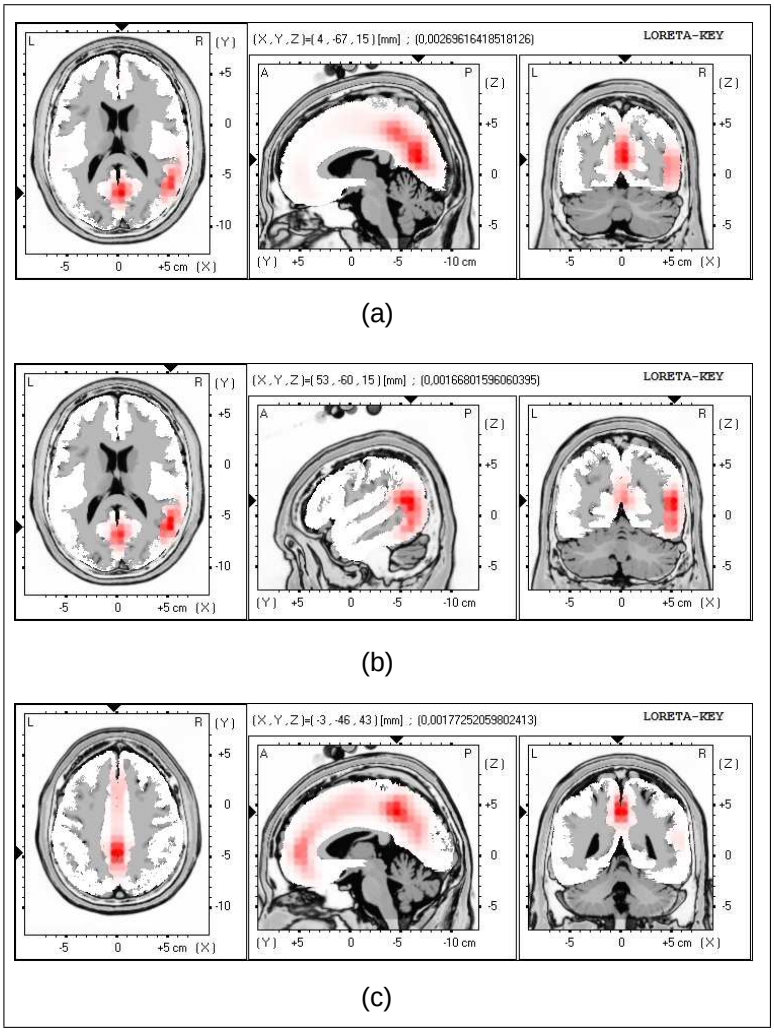

Figure 5.11 LORETA results of (a) raw ERP sequence, and sequences produced from (b) approximation (low spatial frequency) component, (c) detail (low spatial frequency) component of scalp maps of Cluster-6 (445-500 ms).

	TX	TY	TZ								
Raw	4	-67	15	Limbic Lobe	Posterior Cingulate		Separated	TX	TY	TZ	
	53	-60	15	Temporal Lobe	Superior Temporal Gyrus	⇨	Approximation	53	-60	15	Temporal Lobe	Superior Temporal Gyrus
	-3	-46	43	Limbic Lobe	Cingulate Gyrus	⇨	Detail	-3	-46	43	Limbic Lobe	Cingulate Gyrus

Figure 5.12 Locations of three max. activations of raw ERP and its two separated components in Cluster-6.

6. DISCUSSION

In this work, we have segmented 500 ms post-stimulus period of the average ERP recordings, obtained during the Sternberg working memory test, into six different stages (clusters) by Hierarchical Clustering. Each time frame of these clusters was evolved into 2-D scalp map by Biharmonic Spline interpolation. A Spatial Analysis Toolbox was developed based on wavelet transform (Appendix A), which separates the low and high spatial frequency components of scalp maps. Neuronal generator distribution of EEG sequences, which were built up from scalp maps and their separated components of six clusters, were calculated by LORETA.

6.1 Effect of spatial frequency separation on source localization

The most striking finding of this study is the significant separation of source locations in the brain, thanks to spatial frequency separation of the scalp maps on the surface. This result supports the idea that "spatially different frequency components of scalp topologies might have different sources in the brain", which is underlying assumption of the spatial frequency separation in this thesis.

In Figure 4.24.a, which shows the scalp map patterns of 70 to 115 ms post-stimulus period, major posterior activation at right hemisphere and posterior but minor activation at left hemisphere can be seen. Spatial Wavelet Analysis partially separated posterior right hemispheric activation as a low spatial frequency activation (Figure 4.24.b). Remaining patterns include equally diverse two posterior activations which fall into higher spatial frequency part (Figure 4.24.c). LORETA results of raw scalp map patterns in Figure 4.24.a indicate dominant temporal lobe activation (Superior Temporal Gyrus) besides a less obvious occipital lobe activation (Cuneus) in the brain (Figure 5.1.a). Separated low spatial frequency activity patterns in the scalp maps

in Figure 4.24.b correspond to dominant part of the LORETA results as a temporal lobe activation (Figure 5.1.b). Whereas high spatial frequency components correspond to occipital lobe activation. Finally, LORETA in Figure 5.1.b and Figure 5.1.c show that, current density estimations of high and low spatial frequency patterns are clearly separated as they were together in Figure 5.1.a.

Tables 5.2-5.12 show all results including three major sources of raw maps and local maxima of detail and approximation maps. Results of five clusters except cluster-5 indicate that spatial frequency separation also separates source locations in the brain. In other words, spatially different frequency patterns are built up by different sources. In cluster-5, however, LORETA result of spatially high frequency components (Table 5.10) correspond to activation in sub-lobar insula region, which does not have a visible neuronal activation in Figure 5.9.a.

Another interesting finding is that, LORETA found sources of all spatial low frequency components at the Temporal Lobe.

7. CONCLUSION

We aimed to analyze the spatial components of ERP recordings using 2-D Wavelet analysis in order to separate cognitive processes in the brain. It can be concluded as demonstrated in the Chapter 6 that spatial wavelet analysis can be used in the source detection as a useful pre-analyzing technique at inverse problem.

Promising as the results, may be problematic points also arise from cluster analysis, because it uses raw scalp maps and do not consider spatial frequency components which could not be consistent within the cluster. Applying cluster analysis to frequency components could give better results. Besides, replacing the cluster analysis technique (hierarchical clustering) with state based methods such as hidden-markov model may increase the success of our approach.

7.1 Future Work

In the near future, instead of discrete wavelet transform continuous wavelet transform may be used to overcome limitations of discrete transform. Moreover, 3-D wavelet analysis of scalp surface might be a better approach.

APPENDIX A. SPATIAL SCALP MAP ANALYSIS TOOLBOX

This toolbox is developed in MATLAB environment with graphical user interface (GUI). Program can be called by writing "ssma" from the command line in MATLAB. Initially, appropriate ERP recording as a mat file (MATLAB data format) in matrix form such that the size of matrix is [n; m] where n equals to the number of electrodes (30) and m equals to the number of time frames, has to load by file menu (Figure A.1-1). After loading completed, file name and dimensions of matrix will appear (Figure A.1-2). At this point, specific time frame of ERP sequence can be plotted by filling frame number to the "Frame" box (Figure A.1-3) and pressing "Show" button (Figure A.1-4). Now, electrode locations on scalp map with their amplitude knowledge of that time frame shown in color can be seen (Figure A.1-5).

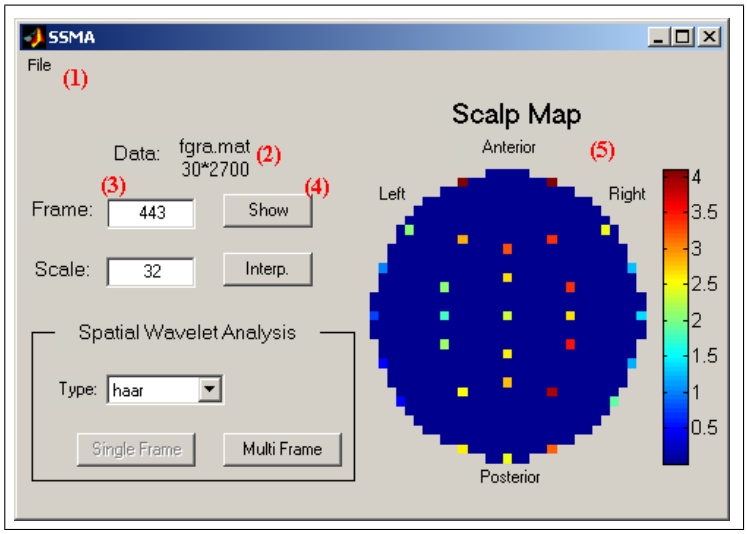

Figure A.1 Time frame plot.

Scalp Maps were attained by the 2-Dimensional interpolation of time frames. According to chosen scale (Figure A.2-6), time frames could be interpolated via pressing "Interp." Button (Figure A.2-7). Increasing the scale produces more smooth scalp maps but increases computation time.

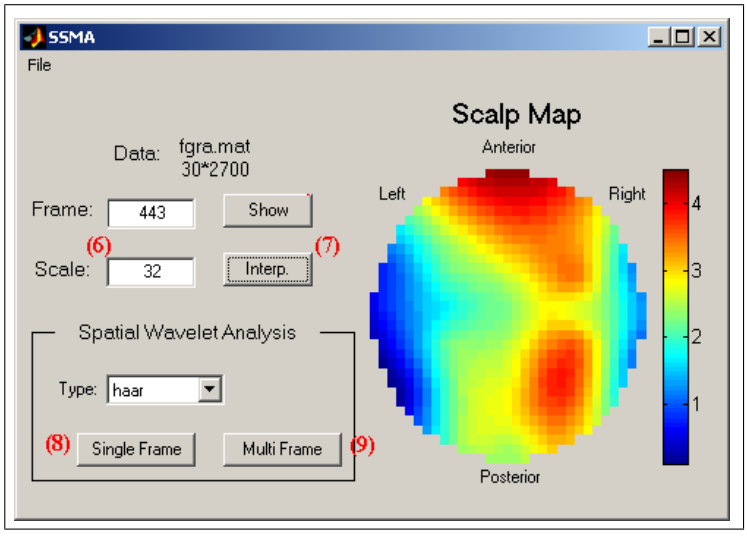

Figure A.2 Interpolated time frame plot.

A.1 Spatial Wavelet Analysis

Seven wavelet types could be used in spatial wavelet analysis with different order choices in SSMA toolbox (Figure A.3). These are: Haar, Daubechies (order: 1, 2, 3, 4, 5, 6), Symlet (order: 2, 3, 4, 5, 6), Coiflet (order: 1, 2, 3, 4, 5), Biorthogonal Spline (order: 1.1, 1.3, 1.5, 2.2, 2.4, 2.6, 2.8, 3.1, 3.3, 3.5, 3.7, 3.9, 4.4, 5.5, 6.8), Reverse Biorthogonal (order: 1.1, 1.3, 1.5, 2.2, 2.4, 2.6, 2.8, 3.1, 3.3, 3.5, 3.7, 3.9, 4.4, 5.5, 6.8), Discrete Meyer Wavelets.

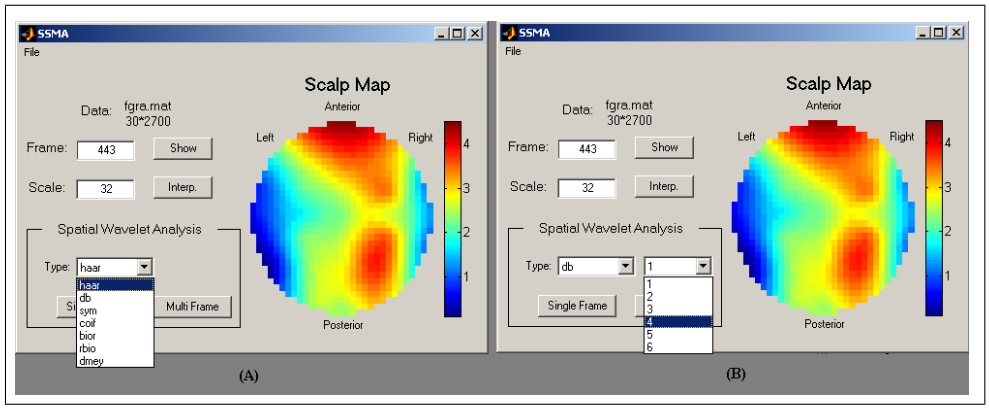

Figure A.3 Wavelet type (A) and order (B) options in the developed toolbox.

"Single Frame" button (Figure A.2-8) is used to start spatial wavelet analysis of a single time frame to find out wavelet type and its order which gives the best

spatial separation results (Figure A.4). In this new window there are three rows and four columns of images. Rows include wavelet coefficients, reconstructed approximation scalp maps, and reconstructed detail scalp maps respectively for each octave (columns).

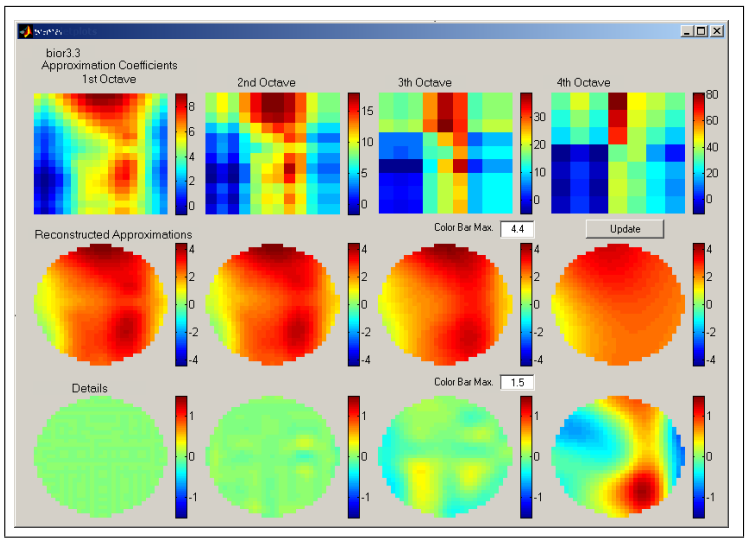

Figure A.4 Wavelet analysis of a single time frame.

"Multi Frame" button (Figure A.2-9) is used to start spatial wavelet analysis of consecutive time frames to compute and plot fourth octave spatial low (approximation) and high (detail) frequencies of raw scalp maps (Figure A.5). In this new window, input file name, matrix dimensions, image scale, wavelet type and octave are shown (Figure A.5-1). Predefined number of time frames (Figure A.5-4), starting point (Figure A.5-2) and step (Figure A.5-3) is used to compute results by pressing "OK" button (Figure A.5-5). Radio buttons are used to select which results will be shown (Figure A.5-6); Details (if "Details" is selected), Approximations (if "Approximations" is selected), and Raw scalp maps (if none of the radio buttons are selected). "Show" button is used to plot scalp maps (Figure A.5-8). Maximum twenty results can be shown in one figure. "<" and ">" buttons (Figure A.5-7) are used to plot previous and next scalp maps. Each scalp map has its time frame number (Figure A.5-9). Plotted scalp maps can be shown as a movie to show the activation changes on the scalp (Figure A.5-10). Right mouse click on a scalp map enables the "save image" button (Figure A.5-11) and that scalp map can be saved as a mat file (3-D matrix).

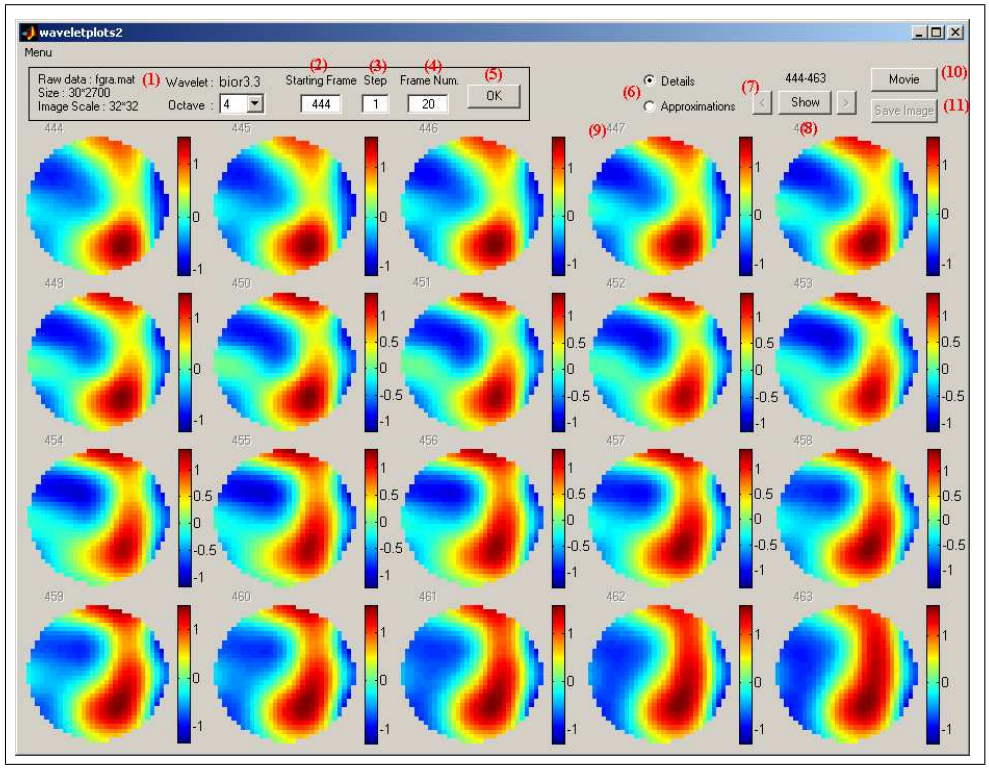

Figure A.5 Wavelet analysis of consecutive time frames.

APPENDIX B. CLUSTERING TOOLBOX

This toolbox is developed in MATLAB environment with graphical user interface (GUI). Program is called by writing "distclust" (because it uses distance measurements during clustering) from the command line in MATLAB. Initially, appropriate ERP recording as a mat file (MATLAB data format) in matrix form such that the size of matrix is [n; m] where n equals to the number of electrodes and m equals to the number of time frames, has to load by file menu (Figure B.1-1). After loading completed, file name and dimensions of matrix will appear (Figure B.1-2).

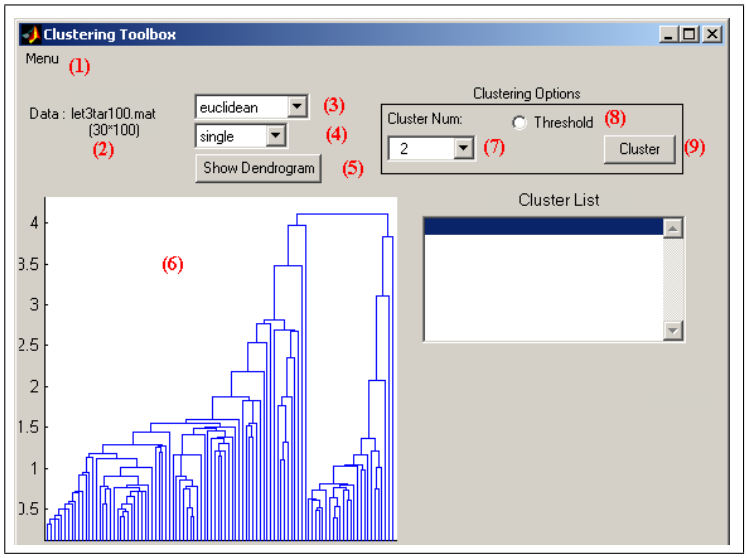

Figure B.1 Clustering Toolbox view

Six distance measurement techniques (Euclidean Distance, Standardized Euclidean Distance, Mahalanobis Distance, City Block Metric, Cosine Distance, Correlation Distance) (Figure B.1-3) with five linking methods (Average, Ward, Complete, Single) (Figure B.1-4) are selectable during clustering analysis with Clustering Toolbox. Now, "Show Dendrogram" button (Figure B.1-5) can be used to plot dendrogram view (Figure B.1-6).

In order to divide dendrogram tree into clusters two options are possible; selecting predefined cluster number or threshold. Cluster number can be selected by a popup

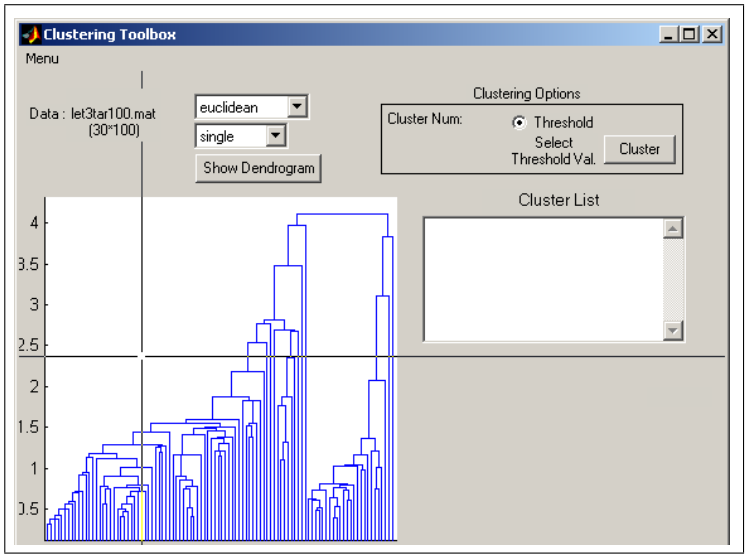

Figure B.2 Clustering Toolbox: Manual threshold selecting.

menu(Figure B.1-7). Threshold can be selected by pressing left mouse button on the dendrogram (Figure B.2)after selecting "Threshold" ratio button(Figure B.1-8). Clustering according to these options can be applied by pressing "Cluster" button (Figure B.1-9). List of clusters will be appear on the list box (Figure B.3-10). If one click on a member of cluster list, that cluster on the dendrogram plot become red (Figure B.3-11), time window of that cluster appears (Figure B.3-12), and average scalp map of that cluster is plotted automatically (Figure B.3-13).

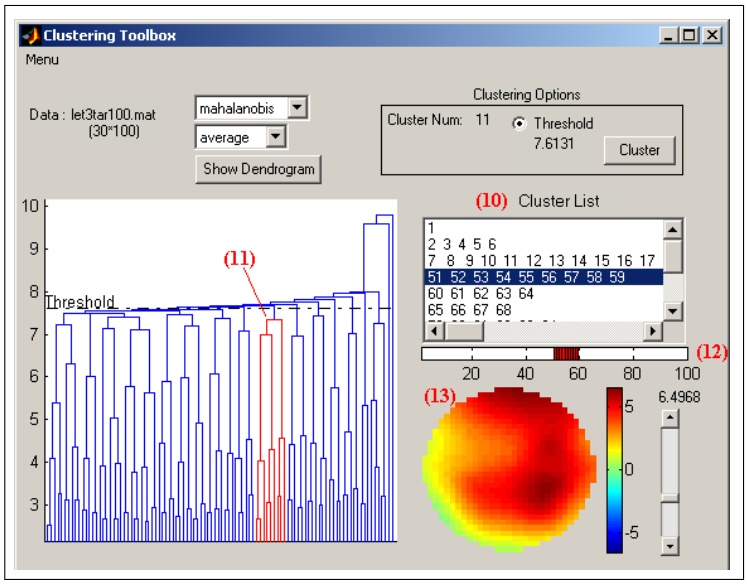

Figure B.3 Clustering Toolbox: Cluster list, Dendrogram view, and Average scalp map plot.

After pressing "Show Dendrogram" button, without applying clustering, branches of dendrogram can be selected by pressing left mouse button, this makes selected branch red, shows members of that branch in "Cluster List" box (Figure B.4).

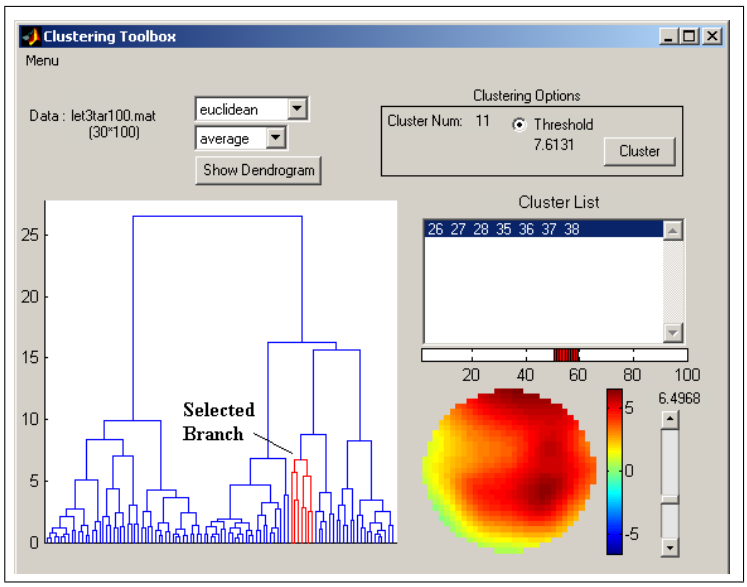

Figure B.4 Clustering Toolbox: Manual cluster selecting.

REFERENCES

1. Halgren, E., "Evoked potentials," in *Neurophysiological Techniques -Applications to Neural Systems* (Boulton, A., G. Baker, and C. Vanderwolf, eds.), Vol. 15 of *Neuromethods*, pp. 147–275, Clifton, N.J.: Humana, 1990.

2. Miller, J., "Discrete versus continuous information processing: Introduction and psychophysiology," *Electroencephalography and Clinical Neurophysiology Supplement*, Vol. 42, pp. 244–259, 1991.

3. Grossman, A., and J. Morlet, "Decomposition of hardy functions into square integrable wavelets of constant shape," *SIAM J Math. Anal.*, Vol. 15, pp. 723–736, 1984.

4. Mallat, S., "A theory for multiresolution signal decomposition: The wavelet representation," *IEEE Transactions on Pattern Analysis and Machine Intelligence*, Vol. 11, pp. 674–693, 1989.

5. Daubechies, I., "Orthonormal bases of compactly supported wavelets," *Comm. in Pure and Applied Math.*, Vol. 41, pp. 909–996, 1988.

6. Ademoğlu, A., *Analysis of averaged and single evoked potentials using damped sinusoids and wavelet basis functions.* PhD thesis, Bogazici University, Istanbul, Turkey, 1998.

7. Ademoğlu, A., T. Demiralp, J. Yordanova, V. Kolev, and M. Devrim, "Decomposition of event-related brain potentials into multicomponents using wavelet transform," *Applied Signal Processing*, Vol. 5, pp. 142–151, 1998.

8. Demiralp, T., J. Yordanova, V. Kolev, A. Ademoğlu, M. Devrim, and V. Samar, "Time-frequency analysis of single-sweep event-related potentials by means of fast wavelet transform," *Brain Lang.*, Vol. 66, pp. 129–145, 1999.

9. Pascual-Marqui, R., C. Michel, and D. Lehmann, "Low resolution electromagnetic tomography: a new method for localizing electrical activity in the brain," *Int J Psychophysiol*, Vol. 18, pp. 49–65, 1994.

10. John W. Clark, J., *The Origin of Biopotentials*, pp. 165–170. Medical Instrumentation Application and Design, New York: John Willey Sons, 3th ed., 1998.

11. Aldroubi, A., and M. Unser, *Wavelets in Medicine and Biology*, Boca Raton: CRC, 1996.

12. Burrus, C. S., R. A. Gopinath, and H. Guo, *Introduction to Wavelets and Wavelet Transforms, a Primer*. Upper Saddle River, NJ (USA): Prentice Hall, 1998.

13. Sheng, Y., "Wavelet transform," in *The transforms and applications handbook* (Poularikas, A. D., ed.), The Electrical Engineering Handbook Series, pp. 747–827, Boca Raton, Fl (USA): CRC, 1996.

14. Kaiser, G., *A Friendly Guide To Wavelets*, Boston: Birkhuser, 1994.

15. Sandwell, D. T., "Biharmonic spline interpolation of geos-3 and seasat altimeter data," *Geophysical Research Letters*, Vol. 2, pp. 139–142, 1987.

16. Wang, K., H. Begleiter, and B. Porjesz, "Spatial enhancement of event-related potentials using multiresolution analysis," *Brain Topography*, Vol. 10, no. 3, pp. 191–200, 1998.

17. Abry, P., *Ondelettes et turbulance*, p. 268. Paris: Diderot ed., 1997.

18. Daubechies, I., *Ten lectures on wavelets*, Vol. 61 of *CBMS*, pp. 117–119. Philadelphia, PA: SIAM, 1994.

19. Pascual-Marqui, R. D., "Review of methods for solving the eeg inverse problem," *Int J Bioelectromagnetism*, Vol. 1, pp. 75–86, 1999.

20. Pascual-Marqui, R. D., D. Lehmann, T. Koenig, K. Kochi, M. Merlo, D. Hell, and M. Koukkou, "Low resolution brain electromagnetic tomography (loreta) functional imaging in acute, neuroleptic- naive, first-episode, productive schizophrenia," *Psychiatry Res*, Vol. 90, p. 169 179, 1999.

21. *LORETA-KEY software package*, The KEY Institute for Brain-Mind Research, Zurich: http://www.unizh.ch/keyinst/NewLORETA/Private/LORETAsetup.exe.